Contrib Mineral Petrol (2011) 162:169–191
DOI 10.1007/s00410-010-0589-9

ORIGINAL PAPER

Melting of carbonated pelites at 8–13 GPa: generating K-rich carbonatites for mantle metasomatism

Daniele Grassi · Max W. Schmidt

Received: 20 May 2010 / Accepted: 20 October 2010 / Published online: 4 November 2010

Abstract The melting behaviour of three carbonated pelites containing 0–1 wt% water was studied at 8 and 13 GPa, 900–1,850°C to define conditions of melting, melt compositions and melting reactions. At 8 GPa, the fluid-absent and dry carbonated pelite solidi locate at 950 and 1,075°C, respectively; >100°C lower than in carbonated basalts and 150–300°C lower than the mantle adiabat. From 8 to 13 GPa, the fluid-present and dry solidi temperatures then increase to 1,150 and 1,325°C for the 1.1 wt% H_2O and the dry composition, respectively. The melting behaviour in the 1.1 wt% H_2O composition changes from fluid-absent at 8 GPa to fluid-present at 13 GPa with the pressure breakdown of phengite and the absence of other hydrous minerals. Melting reactions are controlled by carbonates, and the potassium and hydrous phases present in the subsolidus. The first melts, which composition has been determined by reverse sandwich experiments, are potassium-rich Ca–Fe–Mg-carbonatites, with extreme K_2O/Na_2O wt ratios of up to 42 at 8 GPa. Na is compatible in clinopyroxene with $D_{\mathrm{Na}}^{\mathrm{cpx/carbonatite}} = 10-18$ at the solidus at 8 GPa. The melt K_2O/Na_2O slightly decreases with increasing temperature and degree of melting but strongly decreases from 8 to 13 GPa when K-hollandite extends its stability field to 200°C above the solidus. The compositional array of the sediment-derived carbonatites is congruent with alkali- and CO_2-rich melt or fluid inclusions found in diamonds. The fluid-absent melting of carbonated pelites at 8 GPa contrasts that at $\leq$5 GPa where silicate melts form at lower temperatures than carbonatites. Comparison of our melting temperatures with typical subduction and mantle geotherms shows that melting of carbonated pelites to 400-km depth is only feasible for extremely hot subduction. Nevertheless, melting may occur when subduction slows down or stops and thermal relaxation sets in. Our experiments show that CO_2-metasomatism originating from subducted crust is intimately linked with K-metasomatism at depth of >200 km. As long as the mantle remains adiabatic, low-viscosity carbonatites will rise into the mantle and percolate upwards. In cold subcontinental lithospheric mantle keels, the potassic Ca–Fe–Mg-carbonatites may freeze when reacting with the surrounding mantle leading to potassium-, carbonate/diamond- and incompatible element enriched metasomatized zones, which are most likely at the origin of ultrapotassic magmas such as group II kimberlites.

Keywords Carbonated pelites · Potassium-rich carbonatites · Subduction recycling · Mantle metasomatism · Potassic magmatism

Introduction

Recycling of crustal materials into the mantle occurs through two different subduction-related processes: first, the subducting oceanic crust devolatilizes at least partly

Communicated by H. Keppler.

Electronic supplementary material The online version of this article (doi:10.1007/s00410-010-0589-9) contains supplementary material, which is available to authorized users.

D. Grassi · M. W. Schmidt
Department of Earth Sciences, ETH Zentrum,
8092 Zurich, Switzerland

M. W. Schmidt
e-mail: max.schmidt@erdw.ethz.ch

D. Grassi (✉)
Erdwissenschaften, D-ERDW, Institute of Geochemistry
and Petrology, Clausiusstrasse 25, 8092 Zurich, Switzerland
e-mail: daniele.grassi@alumni.ethz.ch

and produces a mobile phase (which could be a fluid, melt or supercritical liquid, Schmidt et al. 2004; Kessel et al. 2005a, b) thus loosing part of its main and trace element inventory to the mantle wedge. Whatever has been spared and left behind by this fore- and sub-arc process will then be recycled to large depths and ultimately mixed into the mantle. While H_2O is the dominant volatile component in the fore- and sub-arc (Nichols et al. 1994), this is not the case at greater depths. Beyond ca. 9 GPa, after dehydration of lawsonite and phengite (Schmidt and Poli 1998; Ono 1998), only few hydrous phases remain stable, for example, topaz-OH and phase egg in peraluminous sediments (Ono 1998) and hydrous alphabet phases in peridotite (Komabayashi et al. 2004). With depth, these hydrous phases become minor in abundance, and most of the H_2O in the subducting slab becomes stored in nominally anhydrous phases (Hirschmann et al. 2005). In contrast, carbonates, which are refractory at subarc depth (Molina and Poli 2000; Dasgupta et al. 2004; Thomsen and Schmidt 2008a, b), maintain their stability beyond subarc depth conserving most of the CO_2 stored in the subducting lithosphere (Kerrick and Connolly 2001; Connolly 2005).

The strategy to study a carbonated water-poor or dry pelite results from the fact that after the reaction of phengite to K-hollandite near 9 GPa (Domanik and Holloway 1998; Ono 1998) hydrous minerals are limited or absent and flush melting (Poli and Schmidt 2002) of sediments assisted by fluids derived from underlying oceanic basalts or serpentinized peridotites is limited to 9 and 6–7 GPa, respectively (Kawamoto et al. 1996; Schmidt and Poli 1998). Furthermore, sodium becomes compatible in clinopyroxene at ≥3.5 GPa (Schmidt et al. 2004), leaving potassium that strongly depresses the solidus temperature of subducted sediments. Thus, the most fertile composition within the subducting oceanic lithosphere should be CO_2- and K_2O-rich, and melting reactions are expected to be controlled by carbonates and potassic phases.

Although there are a large number of studies on carbonated mafic eclogites (Yaxley and Green 1994; Hammouda 2003; Yaxley and Brey 2004; Dasgupta et al. 2004, 2005, 2006; Litasov and Ohtani 2009; Keshav and Gudfinnsson 2010), there are only three studies on carbonated pelites at upper mantle conditions (Domanik and Holloway 1998; Thomsen and Schmidt 2008a, b). As has been pointed out (Dasgupta et al. 2005; Thomsen and Schmidt 2008b), the melting systematics of peridotites and carbonated K-poor mafic eclogites at 2–7 GPa is similar to the melting relations in the simple $CaCO_3$–$MgCO_3$ ± $FeCO_3$ system (Irving and Wyllie 1975; Buob et al. 2006). This is because Na_2O partitions into clinopyroxene at ≥3.5 GPa, and somewhat simplifying, the silicate components are refractory at ≥3.5 GPa, thus leading to carbonatite initial melts with a few wt% SiO_2 (Dasgupta et al. 2004).

The relation of carbonate and silicate melting is different in K_2O-rich, phengite bearing lithologies (Thomsen and Schmidt 2008b): the addition of H_2O and K_2O lowers the temperature of the fluid-absent silicate solidus to 900–1,150°C (2.5–5 GPa) such that at the solidus silicate melt coexists with high-Mg calcite. The latter then melts out in an almost isothermal reaction at 1,050–1,100°C (2.5–5 GPa) leading to a narrow, ≤50°C temperature interval of coexisting silicate and carbonatite melt. We expect the fluid-absent silicate solidus with its positive Clapeyron slope of ~70°C/GPa to intersect with the almost isothermal carbonate melting reaction at 5–5.5 GPa. Above this pressure, the melting relations of carbonated pelites should be similar to carbonated MORB or peridotite, in that carbonatites form at the solidus.

The scope of this study is to address the mineralogical and geochemical development of carbonated pelites after major dehydration at depths of 250–400 km and to determine the composition of melts derived from carbonated pelites. These carbonatite melts will migrate into the overlying mantle to create strongly enriched metasomatic zones possibly leading to the formation of most diverse geochemical anomalies in the mantle. Furthermore, K_2O- and CO_2-rich metasomatism, as would be produced by carbonated metapelite melts is probably at the origin of group II kimberlites (Wyllie and Sekine 1982; Wyllie 1988; Mitchell 1995; Mitchell 2005) and other ultra-potassic strongly Si-undersaturated magmas. For these reasons, we investigate the melting of three carbonate-saturated pelites at 8 and 13 GPa, H_2O-free, and with small water contents experimentally determine melting conditions and reverse initial melt compositions.

Experimental procedure and analytical technique

Starting material

The hydrous composition (AM) used in this study is the same as that in Thomsen and Schmidt (2008b) and corresponds to a Fe-rich calcareous clay from the Antilles (Plank and Langmuir 1996) simplified in the K_2O–Na_2O–CaO–FeO–MgO–Al_2O_3–SiO_2–H_2O–CO_2 (KNCFMASH–CO_2) system. The other two compositions DG1 and DG2 are synthetic carbonated pelites in the TiKNCFMASH–CO_2 system saturated in coesite/stishovite, kyanite/corundum and carbonates. The starting materials (Table 1) are made of powders of SiO_2, Al_2O_3, TiO_2, MgO, Na_2SiO_3, fayalite, K-feldspar, wollastonite, $Al(OH)_3$, $CaCO_3$ and $MgCO_3$ (pure natural magnesite from Obersdorf; Buob et al. 2006); the latter three components are to introduce the right amounts of H_2O and CO_2. The powders were mixed employing automatical mills and ground to <5 µm.

Table 1 Bulk starting composition (wt%)

	DG1	DG2	AM[a]
SiO_2 (wt%)	55.32	54.63	47.60
TiO_2	0.67	0.63	–
Al_2O_3	21.39	20.23	22.80
FeO_{tot}	5.50	4.86	9.20
MgO	4.15	2.92	2.00
CaO	4.66	5.88	6.80
Na_2O	3.36	3.20	2.40
K_2O	2.36	2.21	3.60
H_2O	Traces[b]	0.00	1.10
CO_2	2.60	4.50	4.80
Tot	100.00	99.07	100.30
X_{CO_2} (molar)	<1.00	1.00	0.64
K_2O/Na_2O (wt%)	0.70	0.69	1.50
Mg#	57.2	52.4	28.1
X_{Mg} (Fe_{tot}) (molar)	0.39	0.30	0.17
X_{Ca} (molar)	0.32	0.43	0.41
Al/(Na + K + 2Ca) (molar)	1.29	1.10	1.13
Al/(Na + K) (molar)	2.65	2.64	2.91

[a] Thomsen and Schmidt (2008a, b)

[b] Subsolidus experiment at 8 GPa includes small amount of phengites

The starting materials were then kept in a desiccator and dried at 110°C before each use (DG1 and AM), but DG1 turned out to contain a small amount of water absorbed from air, producing some minor phengite. Thus, DG2 was mixed, permanently stored in a vacuum oven at 110°C, and did not yield any indication for the presence of H_2O.

Experimental apparatus and sample preparation

Experiments were conducted in a 600-ton Walker-type rocking multi-anvil at 8 and 13 GPa. To improve the attainment of equilibrium and to reduce chemical zonation in the capsules, the whole multi-anvil apparatus was rotated by 180°C during the experiments (Schmidt and Ulmer 2004). The experiments were rotated continuously during the first 30 min and then every 10 min during the remainder of the experiments lasting up to 5 days.

Tungsten carbide cubes with truncation edge lengths of 8 and 11 mm in combination with prefabricated MgO-octaedra of 14 or 18 mm edge length (14/8 and 18/11 assemblies for 13 and 8 GPa, respectively) were used for the experiments. Natural pyrophyllite gaskets were employed. The furnace assemblies consist of a ZrO_2 sleeve, a stepped $LaCrO_3$ heater with inner MgO pieces, and a molybdenum disc or ring between the furnace and the WC cubes. Pressure was calibrated based on the coesite/stishovite (Yagi and Akimoto 1976; Zhang et al. 1996) and forsterite/wadsleyite (Morishima et al. 1994) transitions for the 14/8 assembly, and on the coesite/stishovite and $CaGeO_3$-garnet–perovskite (Susaki et al. 1985) transitions for the 18/11 assembly. Temperature was controlled by a B-type ($Pt_{94}Rh_6/Pt_{70}Rh_{30}$) thermocouple, and no correction for the effect of pressure on the emf was applied. One or two capsules made of Au, $Au_{80}Pd_{20}$, or $Au_{50}Pd_{50}$ with 1.6 or 2 mm outer diameter (at 13 and 8 GPa, respectively) and lengths of approximately 1.5 mm were used in each experiment. Quenching was achieved by turning off the heating power and was followed by pressure unloading of about 15–20 h.

To avoid any loss of the alkali-rich quench phases of the carbonatite melts, capsules were mounted longitudinally in epoxy resin and polished to the centre using a dry polish technique. The open capsules were repeatedly impregnated with low-viscosity resin to avoid the loss of fragments from the quenched carbonatites. After being prepared for analysis, all run charges were kept in a desiccator under vacuum conditions to avoid the formation of whiskers growing on the quenched carbonatites, the former resulting in the destruction of the sample. Equilibrium in the experiments is indicated by well-crystallized grains, 120° triple junctions between phases, and a homogenous composition of the different crystalline phases throughout a particular capsule. Trends of mineral composition as a function of pressure and temperature and mass balance calculations suggest that complete equilibrium was generally reached, at least for the experiments above the solidus.

Analytical methods

All experimental charges were analysed with a JEOL JXA8200 electron microprobe at ETH-Zürich with 15 kV acceleration voltages, 20 nA beam current for silicate minerals and 5 nA for carbonates and carbonatite liquids. Acquisition times were 10 s for Na and K and 20 s for all other elements. Na and K were measured first to avoid diffusional losses. Beam diameters of 1–2 μm were used for all silicate and carbonate phases. Quenched melts were analysed with the most defocused beam possible (3–30 μm). Secondary and back-scattered electron images from the microprobe or from a JEOL JSM6300 field emission SEM were used for textural analysis. Micro-Raman spectroscopy was necessary to identify $CaCO_3$ polymorphs (aragonite), Ti-oxides (TiO_2 with α-PbO_2 structure) and K-hollandite.

Reverse "sandwich experiment" melt composition determination

Carbonatite melts are unquenchable and at low melt fractions form, interstitial melt pools or thin films along capsule walls (Fig. 1), which are almost impossible to properly polish. In addition, quench phases cross the entire melt pools or films, thus measurements could not be performed with a sufficiently defocused electron beam, and contamination by residual mineral phases during the measurement could not be excluded. A focused or only slightly defocused electron beam leads to beam damage in the quench and to alkali loss during measurement. Furthermore, the softness, heterogeneity, small size and reactivity with ambient humidity of the high-alkali carbonate quench material do simply not allow a satisfactory preparation and quantitative analysis of small melt pools. The preferential dissolution and mechanical loss of potassium- and sodium-rich quench during sample preparation leads to a further underestimation of the alkali concentrations which then results in artificially increased concentrations of bivalent cations (especially Ca). Melt compositions obtained under such conditions do not mass balance with the minerals, typically yielding bulks that are alkali deficient with respect to the starting material. Thus, liquid compositions at low degrees of partial melting of the two starting materials DG2 and AM were determined using a reverse "sandwich" procedure (Falloon et al. 1997; Hirschmann and Dasgupta 2007) in which the estimated melt composition from the forward experiments is mixed with the original starting material in order to obtain larger melt pools of a melt saturated in the same phases of the same composition as in the original forward experiment. These large homogeneous areas of melt (Fig. 1e, f) then allow for analysis using a defocused beam (EMPA) or an area scan analysis (SEM). The true melt composition at near solidus conditions is achieved after an iterative process in which the analysed melt composition is employed as an additive to the original starting material in a cascade of consecutive experiments until mineral assemblage (garnet, clinopyroxene, coesite/stishovite, kyanite/corundum ± K-hollandite and carbonates), and mineral compositions in the final sandwich experiment are identical with those in the original melting experiment (forward experiment). Before being mixed with the original starting material, the analysed melts of the original forward experiments and of the different iterations were slightly modified according to both mass balance and partitioning coefficients between solid phases and melt. Secondly, the compositions of the coexisting solid solutions garnet, clinopyroxene, carbonates and K-hollandite in the iterative experiments were compared to the mineral compositions of the original forward experiments to slightly adjust the melt composition such that mineral compositions in the iterative experiments converge with those of the forward experiments. Na_2O concentrations in the carbonatite melt are limited through the saturation with jadeitic clinopyroxene. $\mathrm{Log}\left(D_{\mathrm{Na}}^{\mathrm{cpx/carbonatite}}\right)$ varies linearly with $1/T$, and the obtained Na_2O concentrations of the carbonatite of the final iterative sandwich experiments are in perfect agreement with the $\log\left(D_{\mathrm{Na}}^{\mathrm{cpx/carbonatite}}\right)$ vs. $1/T$ relation determined experimentally at higher temperatures (where larger melt pools allow for direct measurement of the melts in the forward experiments). The potassium content of the carbonatite at 13 GPa is buffered by the presence of K-hollandite as SiO_2 and Al_2O_3 saturation leads to the potassium concentration as the only variable in the solution product of K-hollandite at a given pressure and temperature. At 8 GPa, the K_2O concentration is not strictly buffered, but excessive K_2O contents led to the crystallization of a $K_2Ca(CO_3)_2$ carbonate. The absence of phengite and K-feldspar above the solidus at 8 GPa could have led to a slight overestimation of the total K_2O concentration and K_2O/Na_2O ratio of the melts. Nevertheless, the low amount of melt present in the forward experiments (ca. 10 wt%), in combination with the absence of any major potassium bearing crystalline phase and a low K_2O concentration ≤0.5 wt% in both garnet and clinopyroxene, suggests a K_2O content in the carbonatite higher than 20 wt%. Furthermore, resulting $D_{\mathrm{K}}^{\mathrm{cpx/carbonatite}}$ are roughly constant for temperatures to ca. 200°C above the solidus, indicating, if any, rather an underestimation of K_2O concentrations in the carbonatite liquid.

The iterative procedure was stopped, when the mineral saturations and mineral compositions became identical with those in the forward experiments and the mineral and melt compositions allowed for mass balancing the original bulk composition with deviations ≤2 relative % of each oxide component. Table 2 and Supplementary Table 1 compare the composition of the initially measured melts at a temperature just above the solidus for the two pelites AM and DG2 at 8 GPa (for 13 GPa, see online material) with those obtained after four and five iterative steps, respectively. In these tables, we also give the mass balanced optimized compositions, i.e. after adjusting the K_2O and Na_2O contents of the originally measured melt for an optimal fit. In Fig. 2, we plot the forward experiment melt composition as the 0th iteration step. As can be easily seen, neither the direct initial measurements nor the mass balance-corrected compositions are close to the true equilibrium composition as obtained by the iterative sandwich method. Differences amount to as much as 12 wt% K_2O, 7.5 wt% CaO and 6.5 wt% FeO (Fig. 2), which catastrophically propagate into e.g. K_2O/Na_2O ratios and mass balance in the original forward experiment. For the final melt composition, uncertainties for the alkali concentrations remain relatively high, as the heterogeneous quench of the alkali-rich carbonatite melts causes individual large area analyses to vary considerably.

The results from the reversals on the DG2 and AM melt compositions together with mass balance calculations have then been adopted to adjust the DG1 melt composition.

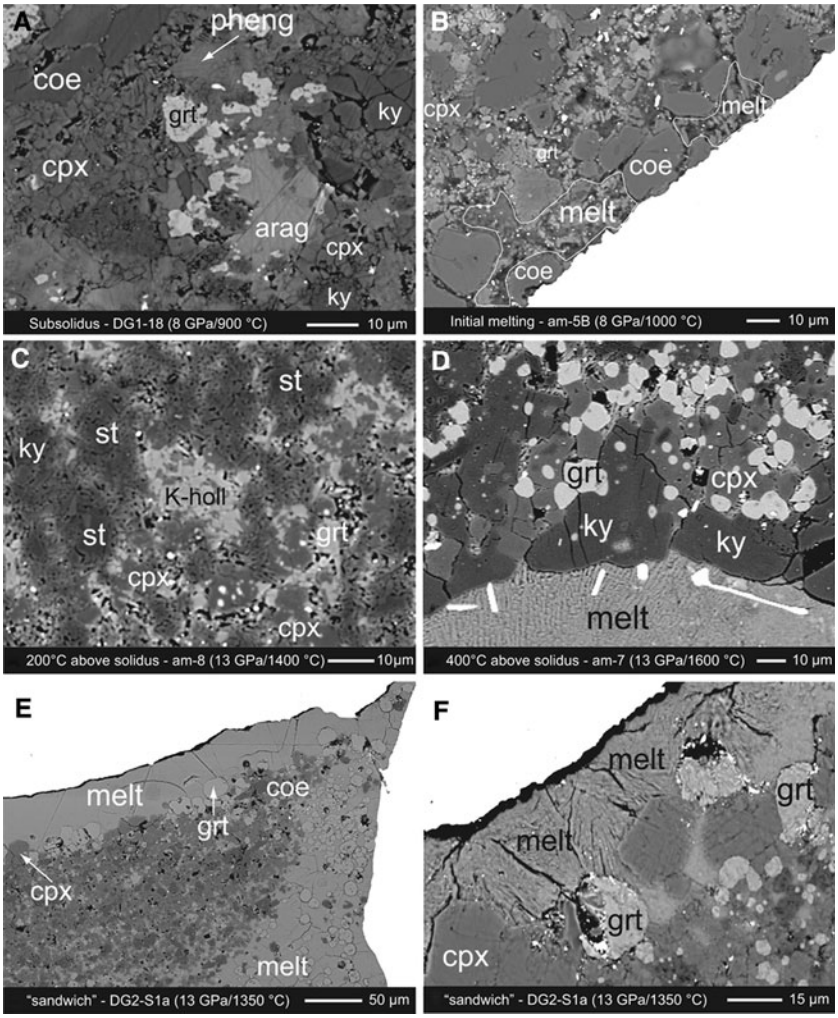

Fig. 1 BSE images of run products. **a** 8 GPa, 900°C, bulk DG1; subsolidus experiment crystallizing a small amount of phengite coexisting with kfsp, grt, cpx, coe, ky, mgs, arag and a Ti-oxide. **b** 8 GPa, 1,000°C, bulk AM; initial melting with the characteristic heterogeneous and small melt pockets which in this case concentrate at the top of the capsule. **c** 13 GPa, 1,400°C, bulk AM; ca. 200°C above the solidus with K-hollandite still stable and coexisting with grt, cpx, st, ky and melt; most of the melt is concentrated along the capsule wall not visible in this image. **d** 13 GPa, 1,600°C, bulk AM; Experiment ca. 400°C above the solidus which still yields a carbonatite melt ($SiO_2 < 10$ wt%) coexisting with grt, cpx, st and ky. **e**,**f** 13 GPa, 1,350°C, bulk DG2; sandwich experiment to reverse melt composition, large amounts of carbonatite melt coexist with grt, cpx, st, ky and K-holl. Phase abbreviations in the figures, text and tables are as follows: *arag* aragonite, *coe* coesite, *cor* corundum, *cpx* clinopyroxene, *dol* dolomite, *grt* garnet, *kfsp* potassium feldspar, *K-holl* K-hollandite, *ky* kyanite, *mgs* magnesite, *pheng* phengite, *stish/st* stishovite

Particularly useful are the partition coefficients (especially $D_{\mathrm{Na}}^{\mathrm{cpx/carbonatite}}$) and the K_2O/Na_2O wt ratio for the potassium and sodium concentrations. The correlation of X^*_{Ca} (bulk) vs. X^*_{Ca} (melt) and X^*_{Mg} (bulk) vs. X^*_{Mg} (melt) is also useful to assess the consistency of analysed and corrected melt compositions.

Results

Thirty experiments were performed on three different bulk compositions (Table 1) at 8 and 13 GPa, and at temperatures between 900 and 1,850°C. Run conditions with calculated phase proportions are listed in Table 3 and represented in Fig. 3. Subsolidus assemblages consist of garnet, jadeitic clinopyroxene, coesite/stishovite, kyanite or corundum, phengite and/or K-feldspar (at 8 GPa) or K-hollandite (at 13 GPa), a Ti-phase and aragonite + Fe-rich magnesite (Fig. 1). Throughout the investigated *P*–*T*-range, the three bulk compositions are all coesite/stishovite-, kyanite/corundum-, garnet- and clinopyroxene-saturated (Fig. 3). The crystallization of a small amount of K-feldspar coexisting with phengite at 8 GPa is taken as proof that the subsolidus experiments and the melting reaction were fluid-absent. The absence of graphite/diamond in the run products suggests an oxygen

Table 2 Near solidus melt composition at 8 GPa for the hydrous (AM) and anhydrous (DG2) pelite

	AM (8 GPa/1,000°C)			DG2 (8 GPa/1,100°C)		
	Synthesis experiment	Mass balance correction	Reverse sandwich after 4 iterative processes	Synthesis experiment	Mass balance correction	Reverse sandwich after 5 iterative processes
Analysis #	7		13	12		15
SiO_2 (wt%)	1.30 (0.9)	0.43	0.30 (0.1)	1.10 (0.6)	0.62	0.26 (0.1)
TiO_2	–	–	–	0.03 (0.1)	0.02	2.37 (0.4)
Al_2O_3	1.17 (0.4)	0.68	1.85 (0.3)	1.27 (0.2)	0.73	1.55 (0.3)
FeO(tot)	5.45 (2.1)	4.10	12.1 (0.9)	6.67 (1.5)	3.97	7.55 (0.6)
MgO	3.60 (1.2)	5.61	2.10 (0.2)	4.22 (2.1)	4.77	2.95 (0.3)
CaO	20.59 (6.2)	10.39	16.5 (0.8)	23.90 (8.5)	15.67	16.3 (1.5)
Na_2O	0.45 (0.1)	0.20	0.65 (0.2)	0.61 (0.5)	0.18	0.95 (0.6)
K_2O	14.94 (5.1)	30.75	26.8 (1.7)	13.04 (9.2)	31.30	24.4 (2.8)
Tot	47.50	52.15	60.30	50.84	57.25	56.33
Si(apfu)[a]	0.05	0.01	0.01	0.04	0.02	0.01
Ti	–	–	–	0.00	0.00	0.05
Al_{tot}	0.05	0.02	0.06	0.05	0.02	0.06
Fe_{tot}	0.17	0.11	0.29	0.19	0.10	0.19
Mg	0.20	0.26	0.09	0.22	0.21	0.14
Ca	0.81	0.35	0.51	0.88	0.49	0.54
Na	0.03	0.01	0.04	0.04	0.01	0.06
K	0.70	1.23	0.99	0.57	1.16	0.96
K_2O/Na_2O (wt%)	32.92	151.81	41.31	21.26	174.88	25.68
Mg#	54	70	23	54	68	42
X^*_{Mg} (Fe_{tot}) (molar)	0.17	0.36	0.10	0.17	0.26	0.16
X^*_{Ca} (molar)	0.69	0.49	0.57	0.68	0.62	0.62

Errors show the variability in the different analysis

[a] Cations calculated on the basis of 6 oxygens

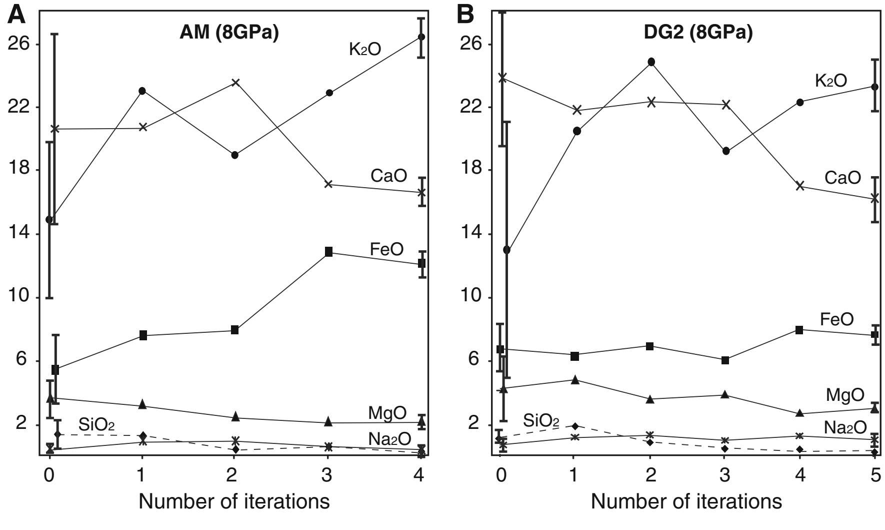

Fig. 2 Composition of carbonatites produced in iterative sandwich experiments in the AM (**a**) and DG2 (**b**) composition at 8 GPa plotted versus iteration number. The composition plotted for the 0th iteration is the one measured in the normal synthesis experiment, corrected for mass balance and then added to the bulk for the first iteration. Note the large errors in particular for K and Ca which are mostly due to the heterogeneity of the quenched carbonatite melts. For details of the iterative sandwich technique, see text

fugacity above the graphite–CO–CO_2 (CCO) buffer. In the following, compositions are discussed in terms of Ca:Fe:Mg ratio which we denote as molar ratio $X^*_{M^{2+}} = M^{2+}/(Ca + Mg + Fe^{2+})$. To avoid confusion, we use Mg# = 100 × Mg/(Mg + Fe^{2+}), also on a molar basis, to describe Mg-Fe^{2+} variations.

Table 3 Experimental run conditions and calculated phase proportions (wt%)

Run no. & bulk	*P* (GPa)	*T* (°C)	Time (h)	Phengite	K-feldspar	K-holl	Aragonite	Magnesite	Dolomite	Ti-Phase[a]	Garnet	Cpx	Kyanite	Cor	Coesite/ stishovite	Carb. melt
DG1-18	8	900	24	x	15.4 (0.7)	–	2.8 (1.5)	7.9 (1.0)	–	x	13.8 (1.7)	30.1 (2.8)	13.5 (1.5)	–	16.5 (0.8)	–
DG1-9	8	1,100	24	–	–	–	–	3.1 (1.1)	–	x	18.2 (1.3)	31.7 (2.5)	17.4 (2.0)	–	21.6 (1.0)	8.0 (3.1)
DG1-11	8	1,200	24	–	–	–	–	1.3 (0.6)	–	–	14.6 (2.6)	34.2 (3.2)	17.7 (1.8)	–	21.5 (1.2)	10.9 (3.0)
DG1-19	8	1,300	24	–	–	–	–	–	–	–	13.4 (2.7)	33.1 (2.6)	18.6 (1.3)	–	22.7 (0.8)	12.2 (2.5)
DG1-13	8	1,400	24	–	–	–	–	–	–	–	10.0 (2.1)	40.7 (2.8)	16.4 (2.8)	–	19.1 (1.0)	13.9 (2.8)
DG2-1	8	900	24	–	xx	–	x	xx	–	x	xx	xx	xx	–	xx	–
DG2-5B	8	1,000	96	–	14.1 (0.8)	–	3.3 (1.0)	6.2 (0.6)	–	x	16.2 (2.1)	31.0 (2.2)	13.9 (1.8)	–	15.3 (1.3)	–
DG2-3	8	1,100	24	–	–	–	–	–	3.2 (1.3)	x	16.4 (1.6)	32.7 (2.9)	15.8 (2.0)	–	24.6 (1.2)	7.4 (3.2)
DG2-2	8	1,250	24	–	–	–	–	–	–	–	16.1 (1.9)	36.2 (2.8)	15.0 (2.8)	–	22.7 (1.0)	10.0 (2.8)
DG2-4	8	1,400	9	–	–	–	–	–	–	–	11.1 (3.4)	31.4 (2.5)	13.8 (1.8)	–	20.6 (0.9)	11.0 (3.1)
am-1	8	900	24	30.4 (1.9)	–	–	5.9 (0.7)	5.4 (1.1)	–	–	18.8 (2.1)	20.8 (2.3)	11.5 (1.7)	–	7.1 (0.8)	–
am-5B	8	1,000	96	–	–	–	x	–	–	–	26.4 (2.4)	22.3 (2.6)	21.2 (2.9)	–	16.9 (1.0)	12.8 (1.7)
am-3	8	1,100	24	–	–	–	x	–	–	–	18.3 (2.1)	24.0 (3.0)	23.1 (2.6)	–	20.4 (1.0)	14.3 (2.1)
am-2	8	1,250	24	–	–	–	–	–	–	–	16.0 (1.6)	26.0 (2.4)	23.1 (1.7)	–	19.9 (1.1)	14.9 (2.8)
am-4	8	1,400	9	–	–	–	–	–	–	–	11.7 (1.6)	28.0 (3.2)	24.2 (2.5)	–	19.7 (0.9)	16.2 (2.3)
DG1-8	13	1,150	24	–	–	16.6 (1.0)	4.15 (0.5)	5.8 (0.8)	–	x	20.9 (1.4)	23.3 (2.7)	–	8.1 (1.5)	21.2 (0.8)	–
DG1-7	13	1,250	24	–	–	9.1 (0.8)	–	2.9 (1.3)	–	x	24.9 (2.8)	20.1 (2.3)	–	9.8 (1.3)	25.8 (1.3)	7.5 (2.7)
DG1-15	13	1,400	24	–	–	–	–	–	–	–	22.9 (1.4)	18.5 (3.1)	20.0 (2.4)	–	26.4 (0.8)	12.2 (2.6)
DG1-1	13	1,600	24	–	–	–	–	–	–	–	21.0 (2.9)	18.3 (2.1)	19.9 (2.9)	–	26.6 (0.8)	14.2 (1.7)
DG1-6	13	1,700	5	–	–	–	–	–	–	–	18.4 (1.4)	18.9 (3.2)	19.7 (1.4)	–	26.8 (1.1)	16.3 (1.2)
DG1-17	13	1,850	1/3	–	–	–	–	–	–	–	2.3 (3.1)	5.6 (2.9)	14.2 (2.9)	–	12.5 (1.0)	65.4 (1.9)
DG2-9	13	1,200	96	–	–	15.3 (0.8)	3.6 (1.2)	6.9 (0.9)	–	x	17.0 (2.1)	25.5 (1.9)	–	7.9 (0.9)	23.8 (2.0)	–
DG2-11	13	1,300	96	–	–	15.2 (0.9)	3.8 (1.6)	6.9 (1.0)	–	x	16.8 (2.6)	24.9 (3.0)	–	7.9 (1.3)	24.4 (1.3)	–
DG2-8	13	1,400	48	–	–	–	–	–	–	–	16.7 (3.3)	18.4 (2.9)	19.3 (2.7)	–	30.7 (1.0)	14.8 (1.3)
DG2-7	13	1,600	24	–	–	–	–	–	–	–	12.7 (1.8)	19.3 (2.0)	21.1 (2.5)	–	31.2 (1.2)	15.7 (1.6)
am-12a	13	1,100	96	–	–	xxx	xx	x	–	–	xx	xx	–	xx	xx	–
am-12d[b]	13	1,100	120	–	–	23.9 (1.1)	6.7 (0.7)	4.2 (0.6)	–	–	18.8 (3.4)	16.9 (3.0)	–	12.5 (0.4)	17.0 (1.3)	–
am-9	13	1,200	96	–	–	17.2 (1.2)	–	–	–	–	25.4 (1.3)	13.6 (2.0)	–	12.4 (1.1)	19.8 (1.2)	11.9 (2.8)
am-11	13	1,300	96	–	–	15.7 (0.9)	–	–	–	–	24.1 (3.4)	13.3 (2.1)	–	14.2 (1.4)	20.7 (1.3)	12.1 (3.0)
am-8	13	1,400	48	–	–	13.3 (0.8)	–	–	–	–	25.6 (2.7)	14.3 (2.1)	18.8 (2.6)	–	14.7 (0.8)	13.3 (2.6)
am-7	13	1,600	24	–	–	–	–	–	–	–	18.0 (2.4)	13.8 (2.0)	25.7 (1.8)	–	23.8 (1.0)	18.6 (2.3)

xxx: >20 wt%; xx: 5–20 wt%; x: <5 wt%

Subsolidus experiments include H_2O and CO_2 as mass balance components. FeO adjusted for Fe loss to the capsule in all experiments with large amount of melt

[a] TiO_2 was excluded during mass balance calculation

[b] This experiment contained 3 wt% H_2O

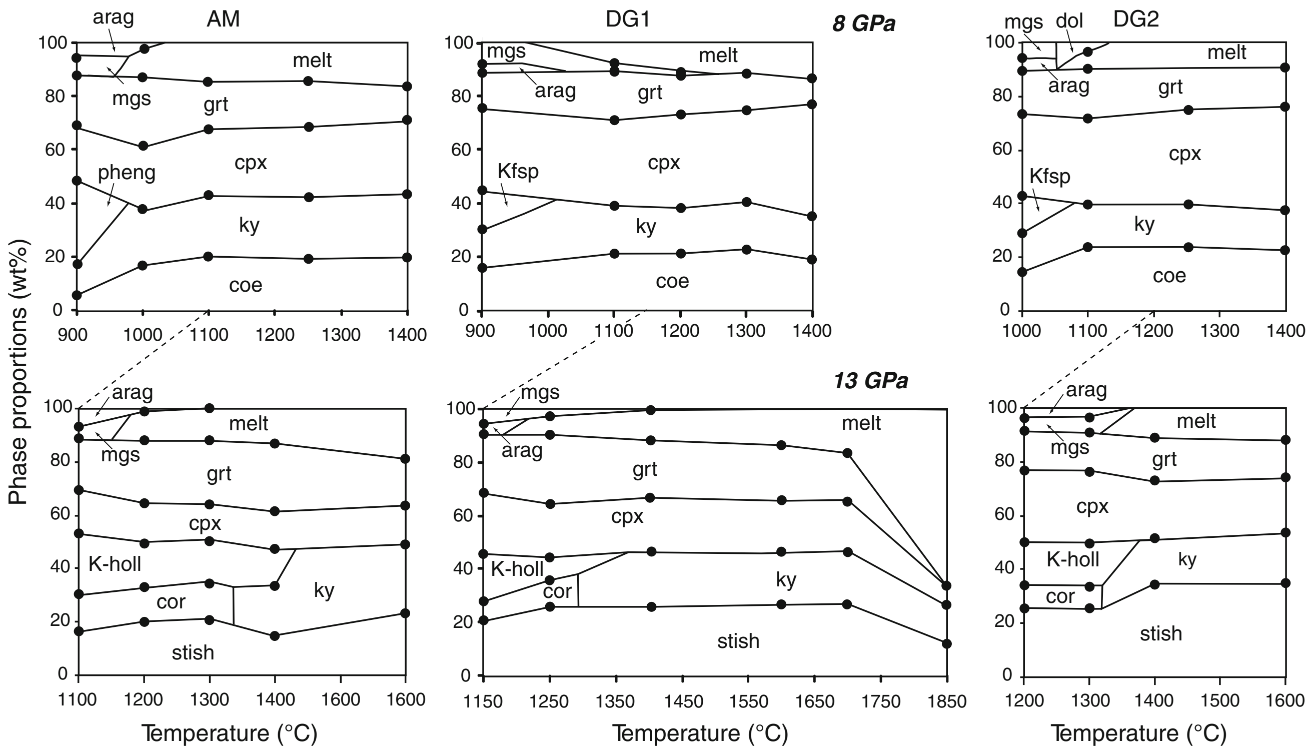

Fig. 3 Calculated modes in weight fractions of the observed phases for coesite/stishovite + kyanite/corundum-saturated, fertile-carbonated metapelites at 8 and 13 GPa. The AM bulk has 1.1 wt% H_2O and a trace of kfsp (not shown) at 8 GPa and 900°C, DG1 has traces of H_2O and minor phengite (not shown) at 8 GPa, 900°C, DG2 is dry. First melts are carbonatites which become silica-rich (see Fig. 4) only at temperatures >400°C above the solidus. At 8 GPa the K-phase completely dissolves into the melt at the solidus while at 13 GPa, K-hollandite may coexist with carbonatite melt up to 200°C above the solidus. To 300°C above the solidus, the melt fraction is just slightly higher than the carbonate fraction in the sediment, larger melt quantities are only produced once melting of the silicate components becomes significant (at 13 GPa for DG1 between 1,700 and 1,850°C)

Solidus location and melt composition

The AM composition, which has 1.1 wt% H_2O and the highest bulk X^*_{Fe} of 0.42, has the lowest solidus temperatures of 950 and 1,150°C at 8 and 13 GPa, respectively. The composition DG1 with minor absorbed H_2O has intermediate solidus temperatures of 1,000 and 1,200°C at 8 and 13 GPa, and as to be expected, the dry DG2 composition has the highest solidus temperatures of 1,075 and 1,325°C at 8 and 13 GPa, respectively (Fig. 4). The temperature differences between the three bulk compositions are mainly due to the different amounts of water present, but are also influenced by their different bulk X^*_{Mg}, X^*_{Ca} and X^*_{Fe}. While all three bulk compositions have magnesite + aragonite at subsolidus conditions, melting consumes magnesite in AM, which has a low X^*_{Mg} of 0.17 and high X^*_{Ca} of 0.41, consumes aragonite in DG1, which has the highest X^*_{Mg} of 0.39 and the lowest X^*_{Ca} of 0.32, leads to dolomite formation in DG2 at 8 GPa, and to exhaustion of both carbonates at the solidus at 13 GPa, a consequence of an intermediate X^*_{Mg} of 0.30 and high X^*_{Ca} of 0.43. Carbonatites formed from the three carbonated pelites are Ca-rich magnesio- (DG1 and DG2) and ferro-carbonatites (AM). They contain 24.4–26.8 wt% K_2O but only 0.65–0.95 wt% Na_2O at the solidus at 8 GPa and 9.4–13.8 wt% K_2O and 4.8–6.2 wt% Na_2O at the solidus at 13 GPa (Table 4; Fig. 5). At 8 GPa, the presence of a small amount of carbonatite melt is enough to immediately dissociate the potassic mineral present, causing the observed extreme K_2O concentrations. In contrast, at 13 GPa, K_2O concentrations are more moderate due to an up to 200°C wide field of coexistence of K-hollandite + carbonatite melt in the H_2O-bearing compositions, and a comparatively high melt productivity exhausting both K-hollandite and carbonates in the dry composition. At 8 GPa, cpx plays a minor role in the melting reaction, whereas at 13 GPa Na_2O contents indicate a strong involvement of cpx in the melting reaction. All solidus melts are poor in SiO_2 (0.2–1.3 wt%) and Al_2O_3 (1.2–2.3 wt%), and contain considerable TiO_2 (0.45–2.37 wt%). The most distinguishing feature in comparison with basalt or peridotite-derived carbonatites are the potassium content and the K_2O/Na_2O wt ratios at the solidus, the latter being as high as 26–42 at 8 GPa, decreasing to 2–2.2 at 13 GPa. This is due to the different K-phases present at 8 and 13 GPa and to the

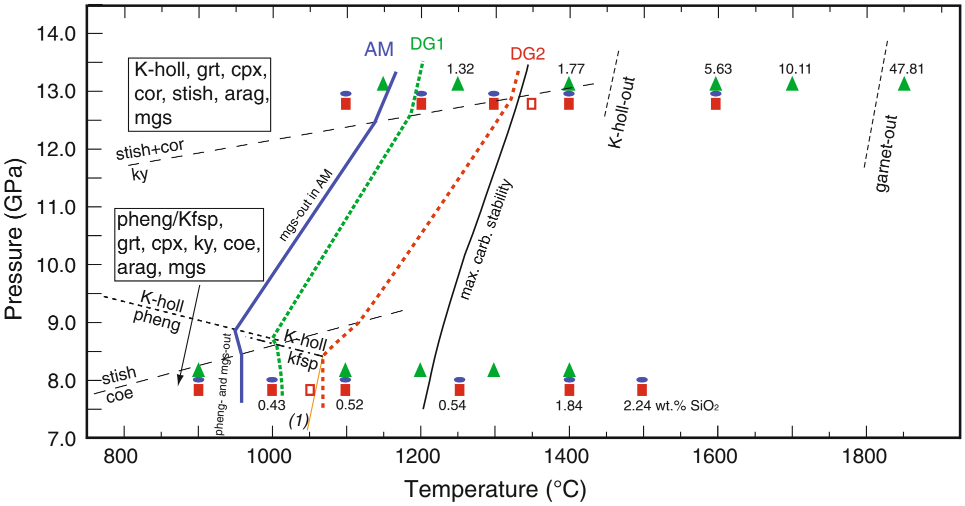

Fig. 4 Pressure–temperature diagram of experimental results for carbonated pelites at 8 and 13 GPa in the system TiKNCFMASH-CO_2. Blue ellipsoids (AM), red squares (DG2) and green triangles (DG1) are individual experiments. The solidus is controlled by the hydrous, alkali and carbonate phases. The AM composition, with 1.1 wt% H_2O is the one with the lowest solidus temperature, followed by the DG1 bulk with traces of water and by the dry DG2 bulk. To define the solidus for AM and DG1, middle points of run bracket temperatures (1,100–1,200 = 1,150°C; 1,150–1,250 = 1,200°C) are chosen; for DG2 at 8 GPa (1,075°C), the solidus is defined by the middle point between the first experiments containing melt (1,100°C) and a reverse experiments at 1,050°C which did not show any sign of melt. Similarly, at 13 GPa, the middle point between the subsolidus experiment at 1,300°C and the reverse experiment at 1,350°C was chosen (for reverse experiments, see Supplementary Table 2). The change of the slope of the different solidi is drawn according to Schreinemaker rules at the intersections with coesite/stishovite reaction (Zhang et al. 1996), the decomposition reaction of kyanite to corundum + stishovite (Schmidt et al. 1997; this study), the phengite to K-hollandite reaction (Schmidt et al. 2004), and the kfsp to K-hollandite reaction. Note that the slope and the exact position of the kfsp to K-hollandite reaction are unknown as in the simple K_2O–Al_2O_3–SiO_2-system K-hollandite replaces wadeite at 9 GPa (at 1,000°C, Yong et al. 2006). Above 8 GPa, the temperature stability of K-hollandite is strongly bulk composition dependent. At 13 GPa, the AM composition with the highest K_2O content has K-hollandite coexisting with the melt to 1,400°C, i.e. 200°C above the solidus; DG1 and DG2 have no K-hollandite above 1,350°C. *Numbers* at *symbols* refer to SiO_2 contents in the melts (in wt%, for the AM bulk at 8 GPa and for DG1 at 13 GPa)

partitioning of Na between clinopyroxene and carbonatite melt (Fig. 6a, b). At 8 GPa, the potassic subsolidus phases phengite and K-feldspar are exhausted at the solidus, and the carbonatite melt becomes the major K-bearing phase. Instead, at 13 GPa, K-hollandite remains stable to as much as 200°C above the solidus. While clinopyroxene is stable in all experiments, the partitioning of Na changes dramatically with pressure: $D_{\mathrm{Na}}^{\mathrm{cpx/carbonatite}}$ (wt%-concentration of Na_2O in cpx divided by the wt%-concentration of Na_2O in the carbonatite) is 10.0–16.1 at the solidus and decreases with temperature at 8 GPa. At 13 GPa, $D_{\mathrm{Na}}^{\mathrm{cpx/carbonatite}}$ varies only between 2.1 and 2.7 (Fig. 6a). The decrease in K_2O/Na_2O with pressure is also accompanied by a decrease in the total amount of alkalis in the near solidus melt from 26–28 to 15–20 wt% at 8–13 GPa, respectively, and consequently by increasing CaO and partly MgO.

The effect of temperature on SiO_2 and Al_2O_3 concentrations in the carbonatites is relatively small, and up to 400°C above the solidus SiO_2 remains at <10 wt%, Al_2O_3 at <5 wt%. It is only from 1,700 to 1,850°C (13 GPa), i.e. 600°C above the solidus, that a silicate melt resembling alkali basalt forms, and that a silicate phase, i.e. garnet, exhausts (Fig. 3). For the investigated pressure and temperature range a continuum from carbonatite towards more silica-rich melts has been observed. No indication of a miscibility gap has been found (Fig. 7), similar to the ≥6 GPa melting of carbonated peridotite (Brey et al. 2008). Other effects of temperature on melt composition are the decrease in CO_2 and K_2O through dilution with increasing melt fraction, and a twofold increase in Na_2O content at 8 GPa, leading to a decrease in K_2O/Na_2O with temperature. At 13 GPa, the K_2O/Na_2O ratio varies only between 2.1 and 4.1 with temperature due to the different behaviour of K-hollandite and clinopyroxene at this pressure.

Textures and mineral compositions

Clinopyroxene (*cpx*) is stable in all experiments and forms relatively small <15-μm-long prismatic crystals. In all isobaric sections, clinopyroxenes have the highest jadeite content at the lowest temperature (Fig. 8; Supplementary Table 3). They then follow various trends leading to a decrease in jadeite and an increase in the diopside, clinoenstatite and Ca-eskolaite endmembers. Ca-Tschermaks component is ≤3 mol% in all experiments, generally

Table 4 Carbonatite melt compositions

Run no. *P* (GPa)/*T* (°C)	am-5B 8/1,000	am-3 8/1,100	am-2[d] 8/1,250	am-4 8/1,400	am-9 13/1,200	am-11[d] 13/1,300	am-8[d] 13/1,400	am-7 13/1,600
SiO_2 (wt%)	0.30 (0.1)	0.55 (0.3)	1.04	3.01 (0.2)	0.48 (0.2)	0.88	1.84	5.45 (0.6)
TiO_2	–	–	–	–	–	–	–	–
Al_2O_3	1.85 (0.3)	2.15 (0.4)	2.23	2.33 (0.3)	1.35 (0.2)	1.94	2.75	3.25 (0.2)
FeO(tot)	12.1 (0.9)	9.9 (0.6)	9.10	8.44 (0.4)	9.50 (0.8)	9.99	9.76	9.8 (0.5)
MgO	2.10 (0.2)	2.35 (0.3)	2.37	2.42 (0.2)	2.32 (0.3)	2.86	3.82	4.19 (0.2)
CaO	16.5 (0.8)	19.2 (1.5)	20.28	20.9 (0.9)	25.5 (1.4)	23.36	21.20	17.4 (1.1)
Na_2O	0.65 (0.2)	1.05 (0.4)	1.20	1.36 (0.5)	4.8 (0.6)	4.76	4.72	4.05 (0.4)
K_2O	26.8 (1.7)	22.5 (1.5)	20.03	17.9 (1.6)	10.2 (1.7)	12.44	15.20	16.8 (1.6)
H_2O[b]	9.40	8.89	8.41	7.97	9.88	8.98	7.21	5.41
CO_2[b]	38.45	37.81	36.12	34.77	43.12	40.12	36.20	23.59
Tot	60.35	57.72	56.25	56.45	54.13	56.23	59.29	60.93
Si (apfu)[a]	0.01	0.02	0.05	0.14	0.02	0.04	0.08	0.23
Ti	–	–	–	–	–	–	–	–
Al	0.09	0.11	0.12	0.13	0.08	0.10	0.14	0.16
Fe_{tot}	0.44	0.38	0.35	0.33	0.38	0.38	0.35	0.34
Mg	0.14	0.16	0.16	0.17	0.16	0.19	0.24	0.26
Ca	0.77	0.93	1.01	1.04	1.30	1.14	0.97	0.78
Na	0.05	0.09	0.11	0.12	0.44	0.42	0.39	0.33
K	1.49	1.30	1.19	1.07	0.62	0.72	0.83	0.90
K_2O/Na_2O (wt%)	41.31	21.43	16.69	13.21	2.13	2.61	3.22	4.15
Mg#	24	30	32	34	30	34	41	43
X^*_{Mg} (Fe_{tot}) (molar)	0.10	0.11	0.11	0.11	0.09	0.11	0.16	0.19
X^*_{Ca} (molar)	0.57	0.64	0.66	0.68	0.71	0.66	0.62	0.56
Compositions of coexisting mineral phases								
Jd (mol%)	71	66	61	55	87	86	84	76
X_{pyrope}	0.12	0.13	0.13	0.14	0.16	0.15	0.16	0.15
$X_{grssular}$	0.36	0.39	0.41	0.41	0.42	0.40	0.41	0.41
D_{Na} (cpx/carb.) (wt%)	16.06	9.38	7.43	5.97	2.71	2.71	2.59	2.63

Run no. *P* (GPa)/*T* (°C)	DG1-9 8/1,100	DG1-11 8/1,200	DG1-19 8/1,300	DG1-13 8/1,400	DG1-7 13/1,250	DG1-15 13/1,400	DG1-1 13/1,600	DG1-6 13/1,700	DG1-17[c] 13/1,850
SiO_2 (wt%)	0.26	2.28	6.84	13.20	1.32	1.77	5.63	10.04	47.82
TiO_2	0.45	1.96	1.88	2.68	1.54	2.79	2.53	2.38	1.01
Al_2O_3	2.03	3.02	3.19	4.81	2.32	1.89	3.64	5.59	16.14
FeO(tot)	7.44	7.95	8.04	7.93	5.17	7.18	6.97	8.15	3.75
MgO	6.78	8.44	8.33	7.87	4.68	5.82	6.19	7.26	5.18
CaO	15.70	17.95	16.21	13.47	20.72	16.10	13.97	13.76	5.68
Na_2O	0.80	1.30	2.06	2.34	6.24	5.95	5.30	5.50	4.01
K_2O	25.13	20.42	16.55	14.20	13.84	14.99	12.74	12.09	3.23
H_2O	n.a.	n.a.	n.a.	n.a.	n.a.	n.a.	n.a.	n.a.	n.a.
CO_2[b]	41.41	36.68	36.90	33.50	44.17	43.51	43.03	35.23	13.18
Tot	58.59	63.32	63.10	66.50	55.83	56.49	56.97	64.77	86.82
Si (apfu)[a]	0.01	0.09	0.28	0.52	0.06	0.08	0.25	0.39	1.49
Ti	0.01	0.06	0.06	0.08	0.05	0.09	0.08	0.07	0.02
Al	0.10	0.14	0.15	0.22	0.12	0.10	0.19	0.26	0.59
Fe_{tot}	0.27	0.27	0.27	0.26	0.19	0.26	0.26	0.27	0.10
Mg	0.43	0.51	0.51	0.46	0.31	0.38	0.40	0.42	0.24
Ca	0.72	0.78	0.71	0.57	0.97	0.75	0.66	0.58	0.19
Na	0.07	0.10	0.16	0.18	0.53	0.50	0.45	0.42	0.24
K	1.38	1.05	0.86	0.71	0.77	0.84	0.71	0.60	0.13

Table 4 continued

Run no.	DG1-9	DG1-11	DG1-19	DG1-13	DG1-7	DG1-15	DG1-1	DG1-6	DG1-17[c]
P (GPa)/*T* (°C)	8/1,100	8/1,200	8/1,300	8/1,400	13/1,250	13/1,400	13/1,600	13/1,700	13/1,850
K_2O/Na_2O (wt%)	31.41	15.71	8.03	6.07	2.22	2.52	2.40	2.20	0.81
Mg#	62	65	65	64	62	59	61	61	71
X^*_{Mg} (Fe_{tot}) (molar)	0.30	0.33	0.34	0.36	0.21	0.27	0.31	0.33	0.46
X^*_{Ca} (molar)	0.51	0.50	0.48	0.44	0.66	0.54	0.50	0.46	0.36
Compositions of coexisting mineral phases									
Jd (mol%)	68	63	63	49	89	84	83	80	65
X_{pyrope}	0.27	0.39	0.45	0.39	0.32	0.39	0.39	0.39	0.51
$X_{grssular}$	0.25	0.17	0.15	0.12	0.26	0.17	0.18	0.17	0.12
D_{Na} (cpx/carb.) (wt%)	12.26	7.21	4.43	2.96	2.06	2.09	2.28	2.05	2.37

Run no.	DG2-3	DG2-2[d]	DG2-4	Reverse	DG2-8	DG2-7
P (GPa)/*T* (°C)	8/1,100	8/1,250	8/1,400	13/1,350	13/1,400	13/1,600
SiO_2 (wt%)	0.26 (0.1)	1.48	1.88 (0.7)	0.22 (0.1)	0.88 (0.4)	2.81 (0.5)
TiO_2	2.37 (0.4)	2.51	3.34 (0.4)	1.83 (0.3)	1.69 (0.3)	2.18 (0.3)
Al_2O_3	1.55 (0.3)	2.05	2.50 (0.3)	1.18 (0.3)	2.06 (0.2)	2.67 (0.2)
FeO(tot)	7.55 (0.6)	6.9	6.27 (0.4)	7.08 (0.6)	8.37 (0.5)	8.8 (0.8)
MgO	2.95 (0.3)	3.89	4.8 (0.5)	5.35 (0.3)	6.06 (0.4)	6.04 (0.3)
CaO	16.3 (1.5)	18.88	20.9 (1.7)	26.4 (1.2)	23.3 (0.9)	21.0 (0.9)
Na_2O	0.95 (0.6)	1.21	1.50 (0.3)	4.71 (0.6)	5.28 (0.8)	4.66 (0.5)
K_2O	24.4 (2.8)	21.68	18.6 (2.1)	9.43 (1.1)	12.6 (1.9)	10.8 (1.8)
H_2O^b	0.00	0.00	0.00	0.00	0.00	0.00
CO_2^b	43.67	42.88	40.21	43.80	39.76	41.04
Tot	100.00	100.00	100.00	100.00	100.00	100.00
Si (apfu)[a]	0.01	0.07	0.08	0.01	0.04	0.12
Ti	0.08	0.08	0.11	0.06	0.05	0.07
Al	0.08	0.11	0.13	0.06	0.10	0.14
Fe_{tot}	0.29	0.26	0.23	0.27	0.29	0.32
Mg	0.20	0.26	0.31	0.36	0.38	0.39
Ca	0.81	0.90	0.98	1.28	1.04	0.97
Na	0.08	0.10	0.13	0.41	0.43	0.39
K	1.44	1.23	1.04	0.54	0.67	0.60
K_2O/Na_2O (wt%)	25.68	17.92	12.41	2.00	2.38	2.31
Mg#	41	50	58	57	56	55
X^*_{Mg} (Fe_{tot}) (molar)	0.16	0.18	0.21	0.19	0.22	0.23
X^*_{Ca} (molar)	0.62	0.64	0.64	0.67	0.61	0.58
Compositions of coexisting mineral phases						
Jd mol%	65	58	55	79	78	78
X_{pyrope}	0.21	0.28	0.30	0.32	0.32	0.33
$X_{grssular}$	0.29	0.26	0.21	0.20	0.20	0.22
D_{Na} (cpx/carb.) (wt%)	10.00	7.11	5.33	2.37	2.32	2.43

n.a. Data not available

[a] Cations calculated on the basis of 6 oxygens

[b] H_2O and CO_2 content calculated from bulk and melt fraction (if no H_2O present CO_2 content calculated by difference to 100 analytical total)

[c] Cations calculated on the basis of 8 oxygens

[d] Melt compositions derived through interpolation of melt compositions at higher and lower temperature and adjusted through mass balance calculations

increasing with temperature. For all three compositions, subsolidus jadeite contents are 68–76 and 80–92 mol% at 8 and 13 GPa. Upon melting at 8 GPa, jadeite contents decrease at most by 5–15 mol% to about 100–200°C above the solidus. Then, cpx becomes omphacitic at 300–400°C above the solidus. Upon melting at 13 GPa, jadeite

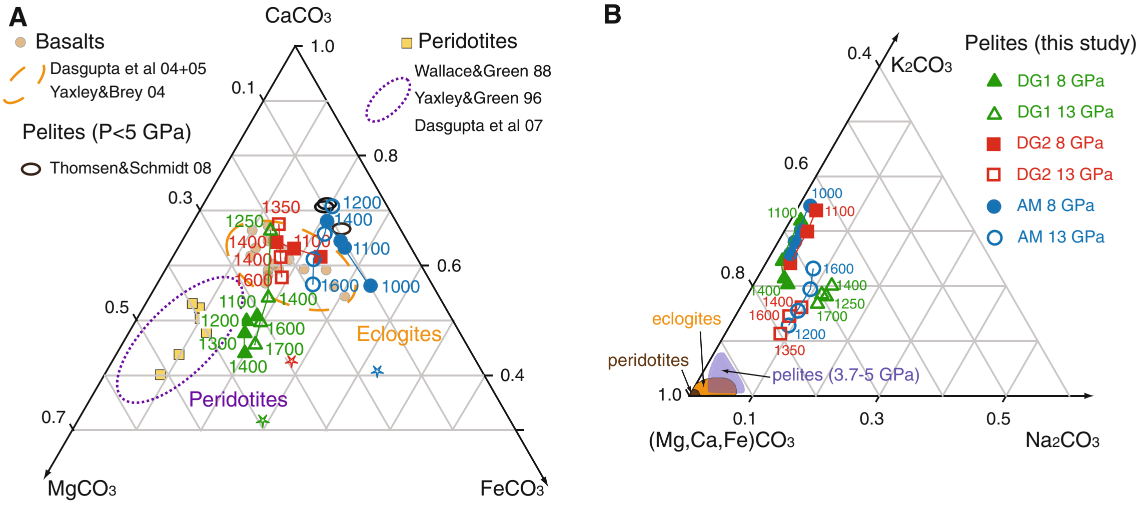

Fig. 5 **a** Compositions of carbonatite melts projected into $FeCO_3$–$CaCO_3$–$MgCO_3$ space. The carbonatites derived from pelites overlap with the carbonatites generated from carbonated mafic eclogites due to similar bulk X^*_{Ca} and X^*_{Mg} (data of Yaxley and Brey 2004; Dasgupta et al. 2004, 2005). Differences between the three pelites reflect bulk composition in terms of X^*_{Ca} and X^*_{Mg}. Note that for each bulk rock type, the near solidus melts plot within relatively narrow fields which are thought to stretch along the minimum cotectic line in the $FeCO_3$–$CaCO_3$–$MgCO_3$ ternary system for pelitic and basaltic bulks, while the near solidus melts from peridotitic compositions stretch along the peritectic of the ternary carbonate system (Franzolin et al. 2010). **b** Compositions of carbonatite melts projected in the Na_2CO_3–K_2CO_3–$(Mg,Ca,Fe)CO_3$ space. The carbonatite melts of this study have much higher amounts of K_2O and Na_2O compared to melts from carbonated mafic eclogites (3–8 GPa, Hammouda 2003; Yaxley and Brey 2004; Dasgupta et al. 2004), peridotites (2–10 GPa, Wallace and Green 1988; Yaxley and Green 1996; Ghosh et al. 2009), and pelites at $p \leq 5$ GPa (Thomsen and Schmidt 2008b). With increasing pressure, the K_2O/Na_2O ratio decreases. The most alkali-rich melts are formed at 8 GPa just above the solidus

contents decrease by 2–3 mol% across the solidus, and by further 2–12 mol% 300–400°C above the solidus. The Ca-eskolaite component increases strongly with temperature from 15–20 to 30–32 mol% at 900–1,200 to 1,250–1,400°C (8 GPa). At 13 GPa, only the DG1 experiment at 1,850°C yielded strongly increased Ca-eskolaite of almost 40 mol%, and in the other two isobaric sections at 13 GPa experimental temperatures were not high enough to achieve such an increase. Generally, Ca-eskolaite decreases with pressure, i.e. from 15–32 to 10–20 mol% from 8 to 13 GPa. K_2O concentrations in cpx vary from 0.20 to 1.03 wt% with the highest values found at 8 GPa at subsolidus conditions.

Carbonates stable in the different experiments are magnesite, aragonite and dolomite. Aragonite and dolomite normally form 5 to 15 μm mostly polyhedral grains, clearly differing from magnesite, which crystallizes as small grains interstitial between larger minerals. Aragonite is almost pure containing less than 1 mol% $FeCO_3$ or $MgCO_3$ component in all bulk compositions. The composition of magnesite (Fig. 9; Supplementary Table 4) reflects the Mg# of the starting materials, while Ca contents generally increase with temperature from 2 to 10 mol%. In DG1 (Mg# 57), magnesite occurs in 5 sub- and super-solidus experiments and contains 16–21 mol% siderite, comparable to what has been found in basaltic eclogites at 4–8 GPa with an Mg# of 64 (Dasgupta et al. 2004). In DG2 (Mg# 52), magnesite has 38 and 30–32 mol% siderite at 8 and 13 GPa, respectively. Finally, in AM (Mg# 28), the magnesite-siderite solid solution has 53 and 64 mol% siderite at 8 and 13 GPa, respectively. In DG2, a Fe-rich dolomite containing 19 mol% siderite component leading to an Mg# of 65.9 is formed at 8 GPa and 1,100°C (DG2). This places the reaction aragonite + ferro-magnesite (Mg# 76.5) = ferro-dolomite (Mg# 65.9) between 1,000 and 1,100°C (8 GPa), which compares well with the 1,100–1,150°C bracket of Luth (2001) in the pure $CaMg(CO_3)_2$ system.

Phengite (*pheng*) is present only at 8 GPa at subsolidus conditions in the two H_2O-bearing bulk compositions DG1 and AM as small (<10 μm) subidiomorphic grains and has, as to be expected (Thomsen and Schmidt 2008b), a high celadonite component of 3.68 Si pfu and an Mg# of 61 in AM (Supplementary Table 5).

K-feldspar (*kfsp*) which occurs at 8 GPa in all subsolidus experiments forms up to 25 μm large, inclusion rich idiomorphic grains almost pure in composition with 0.3–0.4 wt% $Fe_2O_3^{tot}$ and Na_2O- and CaO content close to the detection limit (Supplementary Table 6).

K-hollandite (*K-holl*) is the only potassium mineral at 13 GPa and forms small aggregates of prismatic grains, which contains 0.3–0.7 wt% $Fe_2O_3^{tot}$, 3–6 mol% Na-hollandite, and 2–6 mol% of a Ca component (Supplementary Table 7). The identity of kfsp and K-holl were

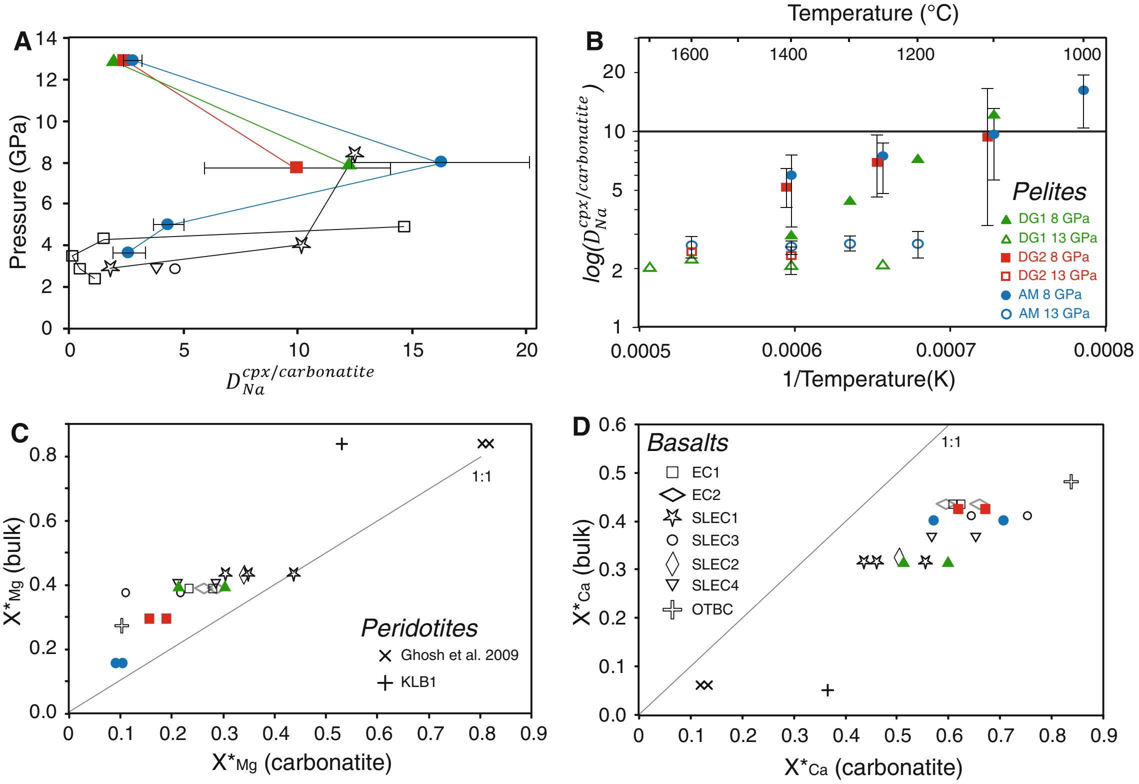

Fig. 6 **a** $D_{\text{Na}}^{\text{cpx/carbonatite}}$ vs. pressure showing an increase in the compatibility of Na_2O in cpx with increasing pressure to 8 GPa reaching a cpx/carbonatite partition coefficient of 16, followed by a decrease down to a value near 2 at 13 GPa when approaching the upper pressure stability of cpx (15–20 GPa). Some data sets, not focused on the carbonatite compositions have inconsistencies probably due to the analytical problem of measuring small intergranular volumes of unquenchable carbonatite melts. **b** Log$\left(D_{\text{Na}}^{\text{cpx/carbonatite}}\right)$ varies linearly with 1/*T*. **c**,**d** X^*_{Ca} (melts) vs. X^*_{Ca} (bulk) and X^*_{Mg} (melts) vs. X^*_{Mg} (bulk) for carbonatites generated from carbonated pelites (this work), mafic eclogites from 2.5 to 8.5 GPa (Hammouda 2003, OTBC; Yaxley and Brey 2004, EC; Dasgupta et al. 2004, 2005, SLEC), and peridotite at 6.6–15 GPa (Dasgupta and Hirschmann 2007; Ghosh et al. 2009). In spite of the strong pressure dependence of the carbonatite melt composition, in particular in the peridotitic system, a positive correlation between bulk X^*_{Ca} and melt X^*_{Ca} and between bulk X^*_{Mg} and melt X^*_{Mg} is evident

confirmed by Raman spectroscopy, although in retrospect, the compositional and textural differences between the two phases as described above would be sufficient for unequivocal identification. In the pure K_2O–Al_2O_3–SiO_2 system, kfsp is replaced by wadeite ($K_2Si_4O_9$) + kyanite + coesite at 6 GPa, which in turn is replaced by K-hollandite at 9 GPa (at 1,000°C, Yong et al. 2006). Wadeite has yet not been found in natural complex systems, and our data indicate a direct transition from kfsp to K-hollandite. The reason for this cannot be the presence of sodium, as extensive $(K,Na)_2Si_4O_9$ solid solution exists (Yong et al. 2006), we thus speculate that Fe_2O_3 stabilizes kfsp over wadeite.

Garnet (*grt*) forms homogenous, mostly inclusion-free subidiomorphic 5–30 µm large crystals. Garnets at subsolidus conditions have similar X_{pyrope} $(Mg/(Mg + Ca + Fe^{2+})$ of 0.10–0.21, and $X_{\text{grossular}}$ $(Ca/(Ca + Mg + Fe^{2+})$ of 0.44–0.47 in AM and DG2 and significantly higher X_{pyrope} of 0.16–0.40, and lower $X_{\text{grossular}}$ of 0.33–0.30 in DG1, mainly reflecting the X^*_{Ca} of the bulk compositions (Fig. 8). In AM, the garnet evolution with temperature is limited, over 500°C, X_{pyrope} increases by 0.06 and $X_{\text{grossular}}$ by 0.03. In DG2, garnet evolves over 400°C through an increase in X_{pyrope} by 0.25 compensated by a decrease in $X_{\text{grossular}}$ by 0.20. Finally, in DG1, X_{pyrope} increases over 500°C by 0.41 and $X_{\text{grossular}}$ decreases by 0.15. The evolution of X_{pyrope} and $X_{\text{grossular}}$ in garnets with increasing temperature (Fig. 10; Supplementary Table 8) does not strongly change with pressure. Na_2O contents in garnets are 0.1–0.45 and 0.65–1.1 wt% at 8 and 13 GPa, respectively, with garnet in the AM bulk always having the lowest concentrations. Si in garnet at 8 GPa remains at ≤3.02 apfu, i.e. no majorite component within error, and amounts to max. 3.08 apfu in garnets from 13 GPa mainly charge compensating for Na through a coupled substitution $M^{2+}Al = Na\ Si$. These Si contents are in stark contrast to garnets from basaltic and peridotitic compositions which at similar conditions typically range from 3.05 to 3.20 Si pfu (Yasuda et al. 1994; Okamoto and Maruyama 2004).

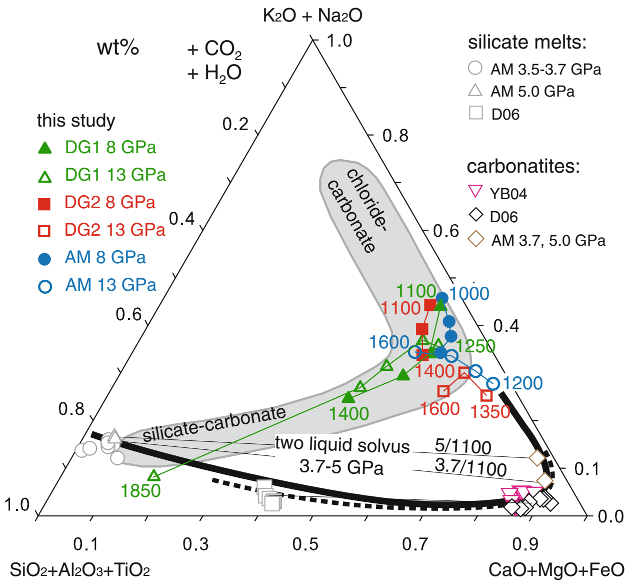

Fig. 7 Pseudo-ternary projection of carbonatite and silicate melts after Freestone and Hamilton 1980), defining a silicate–carbonatite liquid miscibility gap at 1,100°C, 3.7–5 GPa for the AM composition (Thomsen and Schmidt 2008b) compared to the miscibility gap after Dasgupta et al. (2006) (dashed line) and the carbonatites of Yaxley and Brey (2004). At 8–13 GPa, there is a continuum from carbonatite melts towards more silica-rich melts, and no solvus has been observed. The pelite-derived carbonatites are extremely alkali-rich (up to 26 wt%) and $SiO_2 + Al_2O_3$-poor (<15 wt%) to 400°C above the solidus and plot in the same area as carbonate-rich melt/fluid inclusions found in diamonds (Klein-BenDavid et al. 2007, grey field), which however are in part also Cl-rich. The different trends reflect the melting behaviour of the alkali-rich phases at different pressures and the differences in bulk composition. *Coloured lines* connect melt compositions (in a given bulk at a given pressure) with increasing temperature

Nevertheless, this finding is not surprising, as kyanite or corundum-saturated compositions will always result in the minimum majorite content stable at a given pressure and temperature.

Coesite (*coe*) and *stishovite* (*stish*) form anhedral grains that are almost pure in composition with up to 0.5 wt% of FeO^{tot}, increasing with temperature. Similarly, the major impurity of *kyanite* (*ky*) and *corundum* (*cor*) is iron, which amounts to ≤1.1 and ≤5.1 wt% $Fe_2O_3^{tot}$ respectively, increasing with both temperature and pressure.

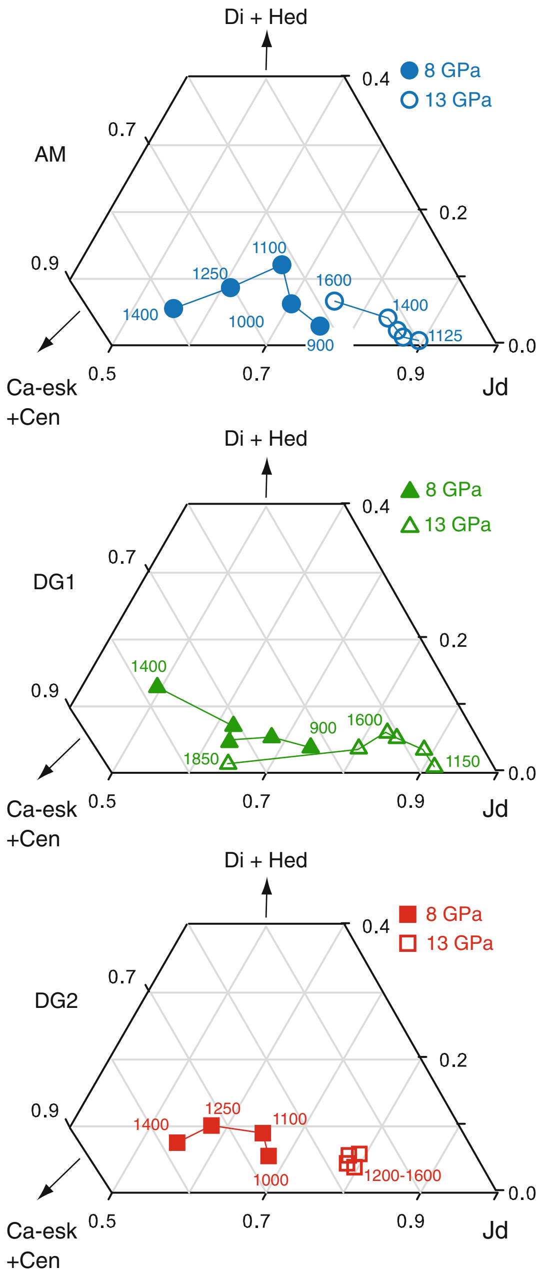

Fig. 8 Clinopyroxene compositions in terms of jadeite (Jd)–diopside + hedenbergite (Di + Hed)–Ca-eskaloite + clinoenstatite (Ca-esk + Cen). With temperature, jadeite contents decrease from $Jd_{74–77}$ (900°C) to $Jd_{49–55}$ (1,400°C) at 8 GPa. The decrease in jadeite content is compensated first by an increase in the diopside and clinoenstatite components followed by a strong increase in the Ca-eskolaite component at higher temperatures. A similar trend is observed at 13 GPa, but shifted to higher jadeite of $Jd_{80–92}$ at the solidus and to lower Ca-eskolaite contents. The Mg# for cpx increases with temperature and decreases with increasing pressure. CaTs component is always <3 mol%

Melting reactions

The presence of kfsp coexisting with phengite at 8 GPa in both hydrous compositions AM and DG1 indicates H_2O-undersaturated, fluid-absent conditions. Similarly, complete absence of phengite in the nominally anhydrous pelite DG2 indicates that this composition is truly dry. At 13 GPa instead, H_2O previously stored in phengite in the AM bulk is likely to be present as a fluid-phase. Nevertheless, the large amounts of K-hollandite, jadeitic cpx and carbonates observed in BSE images of the subsolidus

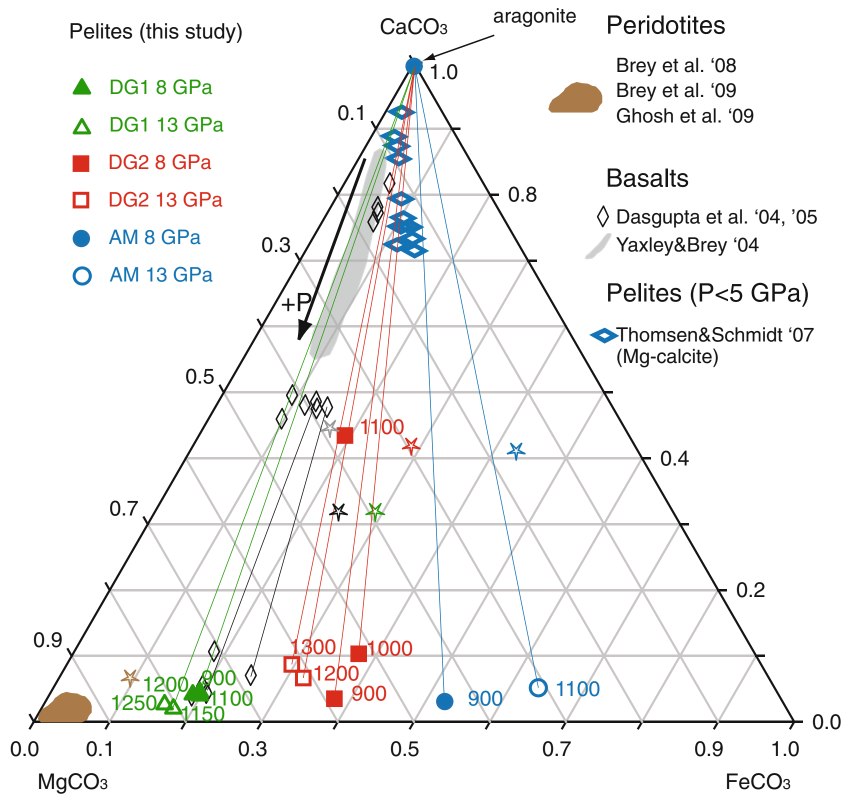

Fig. 9 Carbonate compositions in $CaCO_3$–$MgCO_3$–$FeCO_3$ space. The carbonates of this study are compared to carbonates from carbonated basaltic eclogites (Yaxley and Brey 2004; Dasgupta et al. 2004, 2005), peridotites (Brey et al. 2008, 2009; Ghosh et al. 2009), and sediments (Thomsen and Schmidt 2008b). Note the correlation between carbonate and bulk composition, in particular of the Mg# of magnesite and the bulk. *Tie lines* connect coexisting carbonate pairs, *stars* denote bulk compositions

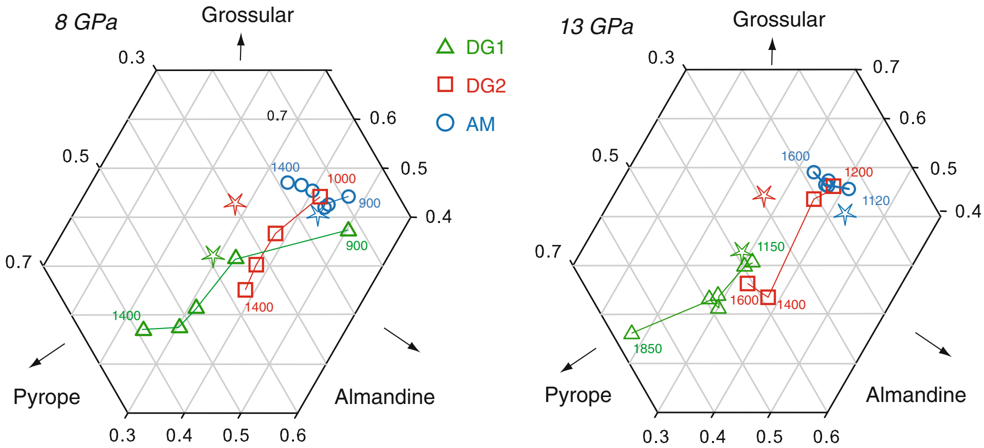

Fig. 10 Garnet compositions. At subsolidus conditions garnets are similar in all three compositions with only small differences in X^*_{Ca}. The different trends with increasing temperature are strongly correlated with bulk composition (especially X^*_{Mg}). In all compositions, garnet shows an increase in the pyrope contents and in Mg# with temperature, this behaviour being more pronounced in the bulk compositions with higher X^*_{Mg}. With increasing pressure similar trends, slightly shifted towards higher pyrope contents, are observed. The majorite component of garnets at 8 GPa is below detection limit, and Si is ≤3.08 apfu at 13 GPa due to saturation in kyanite/corundum. *Stars* denote bulk compositions

experiments at 13 GPa, which are confirmed by mass balance calculations, suggest that the presence of a small amount of fluid does not dissolve major fractions of the potassium-, sodium- or CO_2-bearing phases. Furthermore, the presence and amount of fluid also depends on the H-solubility of other nominally anhydrous phases (Keppler and Smyth 2006) such as stishovite dissolving up to 3,000 ppm H_2O (Litasov et al. 2007) and clinopyroxene (1,200 ppm H_2O in $Di_{60}Jd_{40}$, Wu et al. 2009). The reported high solubility of H in stishovite and cpx suggest that the DG1 composition at 13 GPa could be fluid-absent.

The generation of first highly potassic carbonatite melt at 8 GPa is controlled by a melting out of carbonates and K-phases. The melting reaction is similar for all three bulk compositions with small differences in the amount of each phase involved in the reaction:

$$\begin{aligned}&\mathrm{AM}(900{-}1{,}000^{\circ}\mathrm{C}){:}\\&\quad 0.46\,\mathrm{mgs} + 0.45\,\mathrm{arag} + 2.10\,\mathrm{pheng} + 0.08\,\mathrm{cpx}\\&\qquad = 1\,\mathrm{melt} + 0.87\,\mathrm{grt} + 0.50\,\mathrm{ky} + 0.72\,\mathrm{coe}\end{aligned} \tag{1a}$$

$$\begin{aligned}&\mathrm{DG1}(900{-}1{,}100^{\circ}\mathrm{C}){:}\\&\quad 0.52\,\mathrm{mgs} + 0.35\,\mathrm{arag} + 1.73\,\mathrm{kfsp} + 0.11\,\mathrm{cpx}\\&\qquad = 1\,\mathrm{melt} + 0.47\,\mathrm{grt} + 0.27\,\mathrm{ky} + 0.97\,\mathrm{coe}\end{aligned} \tag{1b}$$

$$\begin{aligned}&\mathrm{DG2}(1{,}000{-}1{,}100^{\circ}\mathrm{C}){:}\\&\quad 0.95\,\mathrm{dol} + 1.71\,\mathrm{kfsp} + 0.13\,\mathrm{cpx}\\&\qquad = 1\,\mathrm{melt} + 0.68\,\mathrm{grt} + 0.21\,\mathrm{ky} + 0.91\,\mathrm{coe}\end{aligned} \tag{1c}$$

the coefficients being in wt-units and normalized to 1 melt. When summarized, this yields the following qualitative reaction:

$$\begin{aligned}&1\,\mathrm{carbonate} + 2\,\mathrm{kfsp\ or\ phengite}(\pm\mathrm{cpx})\\&\quad = 1\,\mathrm{carbonatite} + 0.3\,\mathrm{ky} + 0.9\,\mathrm{coe} + 0.7\,\mathrm{grt}.\end{aligned}$$

The small amount of cpx involved in the reaction and the Na_2O content of <1 wt% of the melts at 8 GPa indicate a minor role of cpx at the solidus. Instead, the complete destabilization of phengite or kfsp at the solidus leads to the crystallization of a large quantity of garnet, kyanite and coesite, the amount of garnet depending on the Mg# of the bulk with the lowest Mg# producing most garnet.

From 8 to 13 GPa, the only mineralogical change is the presence of K-hollandite instead of kfsp or phengite, nevertheless, the situation is quite different: approaching the pressure stability of cpx, jadeite becomes essential during melting as the carbonatite melts at the solidus have 4.7–6.2 wt% Na_2O. Furthermore, K-hollandite now coexists with melt over up to 200°C. Together, this results in a decrease in the K_2O/Na_2O ratio of the melt from 26–42 to 2–2.2, and a decrease in total alkalis from 25.9–27.5 to 14.1–20.1 wt%, from 8 to 13 GPa, respectively. Consequently, the K-phase has a lesser and jadeite a more important role in the mass balanced solidus reactions at 13 GPa:

$$\begin{aligned}&\mathrm{AM}(1{,}100{-}1{,}200^{\circ}\mathrm{C}){:}\\&\quad 0.44\,\mathrm{mgs} + 0.59\,\mathrm{arag} + 0.71\,\mathrm{K\text{-}holl} + 0.36\,\mathrm{cpx}\\&\qquad = 1\,\mathrm{melt} + 0.59\,\mathrm{grt} + 0.08\,\mathrm{cor} + 0.43\,\mathrm{stish}\end{aligned} \tag{2a}$$

$$\begin{aligned}&\mathrm{DG1}(1{,}150{-}1{,}250^{\circ}\mathrm{C}){:}\\&\quad 0.48\,\mathrm{mgs} + 0.46\,\mathrm{arag} + 1.03\,\mathrm{K\text{-}holl} + 0.48\,\mathrm{cpx}\\&\qquad = 1\,\mathrm{melt} + 0.61\,\mathrm{grt} + 0.15\,\mathrm{cor} + 0.69\,\mathrm{stish}\end{aligned} \tag{2b}$$

$$\begin{aligned}&\mathrm{DG2}(1{,}300{-}1{,}400^{\circ}\mathrm{C}){:}\\&\quad 0.52\,\mathrm{mgs} + 0.46\,\mathrm{arag} + 0.69\,\mathrm{K\text{-}holl} + 0.38\,\mathrm{cpx}\\&\qquad = 1\,\mathrm{melt} + 0.50\,\mathrm{grt} + 0.15\,\mathrm{ky} + 0.39\,\mathrm{stish}\end{aligned} \tag{2c}$$

resulting in the average reaction

$$\begin{aligned}&1.0\,\mathrm{carbonate} + 0.8\,\mathrm{K\text{-}holl} + 0.4\,\mathrm{jadeite}\\&\quad = 1\,\mathrm{carbonatite} + 0.6\,\mathrm{grt} + 0.1\,\mathrm{cor/ky} + 0.5\,\mathrm{stish}.\end{aligned}$$

For the AM and DG1 compositions, there is additionally a small amount of H_2O-bearing fluid involved on the educt side. This fluid completely dissolves in the carbonatite; its main effect is the lowering of the solidus temperature. The melting reactions for DG1 and AM bulks at 13 GPa have corundum on the product side because their solidi occur at the high pressure–low temperature side of the reaction 1 stishovite + 1 corundum = 1 kyanite (Schmidt et al. 1997).

Discussion

Effect of bulk composition

The differences in bulk composition are reflected in the position of the solidus and in the amount, composition and evolution of garnet, clinopyroxene, carbonates and melts as function of pressure and temperature. The subsolidus compositions of garnet mostly reflect the X^{*}_{Ca} of the bulk, while the garnet evolution with temperature reflects the bulk X^{*}_{Mg} (Fig. 10). The Mg# of the magnesite-siderite solid solution mainly reflects the Mg# of the bulk (Fig. 9), a lower Mg# correlating with a lower melting point of this carbonate. The higher Na_2O and lower K_2O contents of the DG bulks (3.2–3.4 wt% Na_2O, 2.2–2.4 wt% K_2O) compared to the AM composition (2.4 wt% Na_2O, 3.6 wt% K_2O) is reflected in the higher amount of cpx (30 vs. 20 wt% in the DG vs. AM bulks) and lower amount of K-hollandite (16 vs. 24 wt% in the DG vs. AM bulks) present in the experiments (Table 3). Consequently, K-hollandite has the widest field of coexistence with melt in the AM bulk. Melt compositions also strongly reflect bulk X^{*}_{Mg} and X^{*}_{Ca}, as can be seen when projected into a ternary $FeCO_3$–$CaCO_3$–$MgCO_3$ diagram (Fig. 5a). In our compositions, the effects of bulk X^{*}_{Mg} and X^{*}_{Ca} on the melting temperature cannot be isolated from those of the H_2O and K_2O contents, thought to dominate.

Melting systematics for carbonated lithologies

Compared to other studies on carbonated mafic eclogites (Hammouda 2003; Dasgupta et al. 2004, 2005; Yaxley and Brey 2004) and on peridotites (Dasgupta and Hirschmann 2007; Brey et al. 2008; Ghosh et al. 2009), our pelites exhibit a 100–300°C lower solidus temperature due to the higher alkali (especially K_2O) and water (AM) content (Fig. 11). Even if compared with recent studies on wet carbonated peridotites with high potassium and volatiles content (Brey et al. 2009; Foley et al. 2009) our solidus locates at ca. 100°C lower temperatures due to higher potassium contents and lower X_{Mg}^{*}. Comparing X_{Ca}^{*} and X_{Mg}^{*} of our carbonatites with those formed from carbonated eclogites and peridotites (Fig. 6c, d), it becomes apparent that the carbonatite X_{Mg}^{*} and X_{Ca}^{*} correlates well with the X_{Mg}^{*} and X_{Ca}^{*} of the bulk. Generally, $X_{\mathrm{Ca}}^{*}(\mathrm{melt}) > X_{\mathrm{Ca}}^{*}(\mathrm{bulk})$ and $X_{\mathrm{Mg}}^{*}(\mathrm{melt}) < X_{\mathrm{Mg}}^{*}(\mathrm{bulk})$, and this correlation could be used to predict near solidus melt compositions. The carbonatite melts from our pelites have very similar X_{Mg}^{*} (0.09–0.30) and X_{Ca}^{*} (0.51–0.71) as the melts generated from basaltic eclogites (X_{Mg}^{*} between 0.11 and 0.43; X_{Ca}^{*} between 0.44 and 0.75) but clearly lower X_{Mg}^{*} and higher X_{Ca}^{*} than peridotite-derived carbonatites which have $X_{\mathrm{Mg}}^{*} = 0.53-0.81$ and $X_{\mathrm{Ca}}^{*} = 0.12-0.36$ at similar pressures. Similar to melts from carbonated basaltic eclogites, melts presented in this study at 8 GPa have very low Na_2O contents due to high partition coefficient $D_{\mathrm{Na}}^{\mathrm{cpx/carbonatite}}$ which reaches its maximum near 8 GPa (Fig. 6a). A similar trend can be expected also for carbonated peridotitic systems, but low Na_2O contents in peridotitic cpx combined with the difficulties in obtaining accurate analysis of alkalis in carbonatites led to unrealistic wide ranges of $D_{\mathrm{Na}}^{\mathrm{cpx/carbonatite}}$ (Fig. 8 in Dasgupta et al. 2005). The SiO_2 and Al_2O_3 content in the carbonatites of this study remains below 10 wt% even at 400°C above the solidus. Carbonatites derived from peridotitic and basaltic systems at similar pressure (Dalton and Presnall 1998; Dasgupta et al. 2004; Brey et al. 2008) show much higher SiO_2 and Al_2O_3 contents up to 25–30 wt% at <200°C above the solidus. The most evident reason for this behaviour is the lower solidus temperature on pelitic alkali-rich systems compared to basaltic or peridotitic lithologies. Nevertheless, even in experiments run at similar pressure and temperature conditions, the silica content in alkali-rich carbonatites derived from sediments shows considerably lower values than that in other systems. Silica dissolution in carbonatites coexisting with peridotitic or basaltic assemblages with comparatively low SiO_2 activity is apparently more effective than in carbonatites coexisting with SiO_2-saturated solid assemblages. The principal structural unit of carbonatite melts are isolated planar CO_3-units (Genge et al. 1995; Kohara et al. 1998), not dissimilar to the high concentration of isolated SiO_4 tetrahedra in depolymerized low SiO_2 silicate melts, but contrasting high SiO_2 melts with large clusters or networks of Si tetrahedra. We thus speculate that the high SiO_2 contents in carbonatites of silica undersaturated systems could be a result of the higher structural similarity of carbonatite melt with low Si activity depolymerized silicate melts.

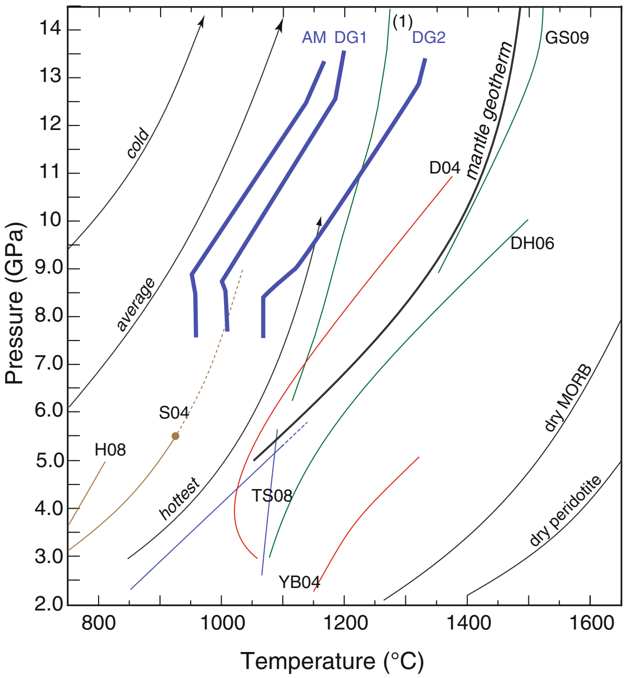

Fig. 11 *P–T* diagram showing a plausible range of subduction *P–T*-paths and solidi for (carbonated) pelites, basalts and peridotites. Comparison of our solidus temperatures with typical subduction paths (Kincaid and Sacks 1997; van Keken et al. 2002; Peacock 2003) and the mantle geotherm (Akaogi et al. 1989) yields melting of these pelites only feasible during very hot subduction or at the end of convergence when subduction halts and thermal relaxation towards the mantle adiabat may occur. *(1)* is the solidus of potassium-rich hydrous carbonated peridotite compiled from Ghosh et al. (2009), Foley et al. (2009) and Brey et al. (2009). Note that the curve GS09 of Ghosh et al. (2009) denotes the carbonate-out of a K-bearing peridotite, but that Ghosh et al. (2009) argue for a solidus at ca. 200°C lower temperature. K-rich carbonatites from subducted sediments, that rise into the mantle are expected to remain in the liquid state also in the mantle at least until major reduction to diamond occurs. *Lines*: solidi of subducted material, *brown*: CO_2-free pelites, *blue*: carbonated pelites, *red*: carbonated MORB, *green*: carbonated peridotite. TS08: carbonated pelite (AM composition) solidus and calcite-out reaction after Thomsen and Schmidt (2008b). D04, YB04: solidi of carbonated basaltic eclogite after Dasgupta et al. (2004) and Yaxley and Brey (2004), the former bulk yields subsolidus dolomite or magnesite, the latter Mg-calcite. D06, GS09: solidi of dry carbonated peridotite after Dasgupta and Hirschmann (2006) and Ghosh et al. (2009). S04 and H08: melting and dissolution curves for potassium-rich wet sediments after Schmidt et al. (2004) and Hermann and Spandler (2008). The solidus for dry peridotite is after Hirschmann (2000) and the one for dry MORB after Yasuda et al. (1994)

The carbonated pelite solidus, slab melting and the role of thermal relaxation

A comparison of calculated subduction geotherms (Kincaid and Sacks 1997; van Keken et al. 2002) with the solidus of carbonated pelites yields the following picture. With respect to the dry solidus (DG2) of carbonated pelite, melting is only feasible for extremely hot subduction

(Fig. 11) over a small pressure window at 7–9 GPa. While carbonated pelites might melt under these conditions, carbonated mafic eclogites or peridotites will not (Fig. 11). In a system with 1.1 wt% H_2O, such as the AM composition, the solidus is lowered by $\geq$100°C, and melting could take place at temperatures close to average subduction zone conditions at pressures $\geq$7–9 GPa. The slope of the AM solidus is subparallel to a typical *P–T* trajectory, implying that melt would form upon crossing of the *P–T* trajectory, but that upon further burial, no significant further melt production would occur. At $\geq$9 GPa, the AM composition has ca. 1 wt% free H_2O supposedly forming a H_2O–CO_2-fluid, causing the previously fluid-absent carbonated pelite to become fluid-present. It is questionable whether this fluid would be preserved in the carbonated pelite during further subduction at pressures above the phengite dehydration. If this fluid is not retained in the pelite, then, melting has either to occur immediately at the phengite decomposition reaction, or the H_2O-bearing fluid would be lost to the overlying mantle wedge. The further subducting pelite becomes thus dry. and the solidus of the dry DG2 composition would apply. Cold subduction *P–T*-paths will not allow melting of carbonated pelites during ongoing subduction.

The precision of temperature prediction in subduction zones does not allow defining an exact depth of melting for the carbonated pelites, in particular near the slab surface, where sediments locate at least when oceanic crust enters into a subduction zone. Nevertheless, the three solidi are 150–300°C below the mantle adiabat. Thermal relaxation of the slab towards the adiabat becomes important with the end of surface convergence, when subduction slows down or stops due to collision or changes in plate configuration, possibly leading to slab break off. Progressive temperature increase will promote at first the melting of the most fertile lithologies, i.e. hydrous and dry carbonated pelites. These melts will travel into the surrounding mantle leaving a volatile-free, potassium-poor, peraluminous restitic eclogite assemblage behind. This assemblage would be refractory and may survive within the mantle for long periods without being affected by other melting events.

Our experiments were performed under closed system conditions. In nature, it can be expected that, once formed, carbonatite melts rapidly escape from their source rock. Thus, when the solidus reaction is completed due to carbonate exhaustion, further melting of the residual volatile-free K_2O-poor eclogitic restite can only be expected when reaching the volatile-free solidus of SiO_2-saturated eclogites.

H_2O at $\geq$9 GPa in CO_2-free pelites

Previous studies on SiO_2–Al_2O_3-saturated compositions at similar *P–T*-conditions resulted in two hydrous phases at pressure above the phengite to K-hollandite reaction at 8–9 GPa: Ono (1998) studied average shale and continental crust compositions with 6 wt% H_2O at 6–15 GPa, 800–1,400°C and found, that in peraluminous compositions topaz-OH ($Al_2Si_4(OH)_2$, Wunder et al. 1993) forms instead of kyanite upon phengite breakdown. Nearly 12 GPa topaz-OH reacts to phase egg ($AlSiO_3(OH)$, Eggleton et al. 1978; Schmidt et al. 1998). Although phase egg is stable to 22 GPa in synthetic Al_2O_3–SiO_2–H_2O systems (Sano et al. 2003), its temperature stability in natural systems appears to be limited to between 1,300 and 1,400°C (Ono 1998). Dobrzhinetskaya and Green (2007) confirmed the presence of K-hollandite and topaz-OH in continental crust compositions at 10–12 GPa, 1,100–1,300°C. At 16–20 GPa, 1,250–1,300°C, Rapp et al. (2008) obtained phase egg in a pelitic bulk composition with 8 wt% H_2O, but not in the one with 1 wt% H_2O. Even in the original synthesis by Eggleton et al. (1978), phase egg was only obtained from starting materials containing substantial quantities of water. Our subsolidus experiments at 13 GPa, which locate in the phase egg stability field, did not yield phase egg in the AM bulk with 1.1 wt% H_2O. A repetition of one experiment at 13 GPa, 1,100°C with ca. 3 wt% H_2O confirms the previous observations that phase egg only crystallizes in pelitic compositions if larger amounts of water (>5 wt%) are present. Realistically, subducting slabs at >9 GPa, contain less than the 1.1 wt% H_2O as present in our AM composition or in the 1 wt% H_2O composition of Rapp et al. (2008). Topaz-OH may be formed at the phengite to K-hollandite reaction at $\leq$1,000°C. At higher temperatures, a supercritical liquid results which is expected to mostly escape the system, leaving <0.1 wt% H_2O that may be incorporated into nominally anhydrous minerals (Keppler and Smyth 2006; Litasov et al. 2007; Wu et al. 2009).

Evidence for subducted carbonates and K-rich metasomatism in the mantle

The analysis of melt and fluid inclusions in diamonds and other minerals found in kimberlites generated deep in the mantle (van Achterbergh et al. 2003; Kamenetsky et al. 2004; Korsakov and Hermann 2006; Tomlinson et al. 2006; Klein-BenDavid et al. 2007; Guzmics et al. 2008) yielded compositions very similar to our experimental alkaline carbonatites. These inclusions are extremely rich in alkalis, with generally $K_2O > Na_2O$, and also in volatiles (Cl, H_2O and CO_2), and show a strong affinity to the cationic composition of our melts, especially the carbonate-rich end members (Fig. 7). Not only fluid and melt inclusions but also many mineral inclusions in diamonds (Kamenetsky et al. 2004; Walter et al. 2008) show a correlation with the phases in which our melts are saturated (carbonates, hydrous and potassium-rich phases, K-hollandite, corundum and stishovite). Trace elements and O, C and Sr isotopic signatures of carbonatite inclusions in kimberlitic minerals suggest a crustal or crust-derived metasomatic provenance of these materials (van Achterbergh et al. 2002; van Achterbergh et al. 2003; Cartigny 2005).

Mantle metasomatism and origin of ultra-potassic (UP) volcanism

The solidus for carbonated, wet and K_2O-rich peridotites lies at temperatures between 1,100 and 1,200°C at oxidizing conditions from 8 to 13 GPa (Ghosh et al. 2009; Brey et al. 2009; Foley et al. 2009) which is about 200°C below the average mantle geotherm (Akaogi et al. 1989; Fig. 11). With the end of surface plate convergence, a decreasing burial rate of the slab results in a relaxation of subduction isotherms which in turn causes the melting of the most fertile lithologies within the slab. As temperatures increase, the carbonated pelites situated at the upper part of the slab column will melt and generate highly mobile carbonatites (Hammouda and Laporte 2000), in our case alkali-rich carbonatite melts with $K_2O \gg Na_2O$. As long as temperatures remain at $\geq$1,100–1,200°C, these carbonatites will infiltrate into the overlying mantle and quickly percolate upwards, thereby concomitantly introducing large amounts of CO_2 and K_2O. The absence of any evidence for an accumulation of this kind of melts at the base of the lithosphere, where temperatures would be low enough for complete crystallization of the carbonatite melts, suggests that a redox reaction with the reduced mantle (Frost and McCammon 2008; Rohrbach et al. 2009) immobilizes these carbonatites. In fact, diamond crystallization has been shown to be favored by the catalytic behaviour of K_2CO_3-rich melt and fluid (Taniguchi et al. 1996; Palyanov et al. 2007; Klein-BenDavid et al. 2007).

The interaction between incompatible elements, potassium and calcium with the mantle will transform the latter's assemblages, introducing incompatible elements, causing an increase in the clinopyroxene/orthopyroxene ratio (Green and Wallace 1988; Thibault et al. 1992; Dalton and Wood 1993), and the crystallization of carbonate and potassic phases such as magnesite, K-rich carbonate, phlogopite, K-richterite and phase-X (Konzett and Fei 2000). With increasing distance from percolation zones, this process will produce carbonated wehrlites, carbonated re-fertilized lherzolites and so-dubbed "cryptic" metasomatism (Dawson 1984). Later melting of these metasomatic enriched mantle veins (Foley 1992) and domains will produce alkali-rich carbonatites with high concentrations of incompatible elements and a hybrid mantle/crust geochemical characteristics. These carbonatites may then evolve to the different highly alkaline ultrapotassic silicate melts that form group II kimberlites, lamproites and aillikites (Foley et al. 2009; Brey et al. 2009; Francis and Patterson 2009). Geochemical data of many alkali rocks, associated carbonatites, and of kimberlites and related rocks show isotopical characteristics on the mixing line between the HIMU (recycled altered oceanic crust) and EM1 (subducted oceanic crust and pelagic sediments) mantle endmembers (Faure 2000; Becker and Le Roex 2006). These characteristics are thought to be generated by low degree melting of a depleted mantle re-enriched through a potassic-, CO_2 and incompatible element-rich melt or fluid (Girnis et al. 2006; Becker and Le Roex 2006; Brey et al. 2008; Agashev et al. 2008). All these characteristics coincide with our pelite-derived alkaline carbonatites. The potassium- and CO_2-dominated metasomatism initiating with the melting of carbonated pelites at $\geq$8 GPa would cover most of the important geochemical characteristics deduced for the generation of ultrapotassic and related rocks in the deep upper mantle.

Application for the genesis of group II kimberlites

Kimberlites are ultrapotassic, ultramafic and at the same time extremely enriched in most of the incompatible trace elements and volatile including CO_2 and H_2O. Both kimberlite groups (group I and group II) are thought to be generated at pressure higher than 5–6 GPa from a depleted mantle source re-enriched through volatile-rich melts or fluids containing high trace elements concentrations (Brey et al. 2008). Group II kimberlites differ from group I in their mineralogy, major and trace elements concentrations and isotopic composition (Mitchell 1995; Becker and Le Roex 2006). Trace element characteristics of group II kimberlites show an affinity to calc-alkaline mafic magmas and thus to subduction-related fluids and melts (Coe et al. 2008). Moreover, their Hf, Sr and Nd isotopic compositions with low εHf, εNd and highly radiogenic $^{87}Sr/^{86}Sr$ (Mitchell 1995; Becker and Le Roex 2006; Coe et al. 2008) match well with the one of ancient sediments (Rehkamper and Hofmann 1997; Vervoort and Blichert-Toft 1999). Compared to group I kimberlites, group II kimberlites are characterized by higher K_2O and H_2O contents, higher K_2O/TiO_2- and K_2O/Na_2O (Fig. 12) ratios and higher CaO for a given SiO_2 concentration (Mitchell 1995; Becker and Le Roex 2006).

McCandless (1999) presented a model where kimberlitic magmatism was attributed to deep-seated subduction, based on age data for kimberlite magmatism combined with seismic images and thermal models of subducted slabs. Our carbonatite melts generated from a phengite bearing carbonated pelite at 8 GPa is able to explain all these observed characteristics of group II kimberlites. They contain large amounts of volatiles (CO_2 and H_2O), are

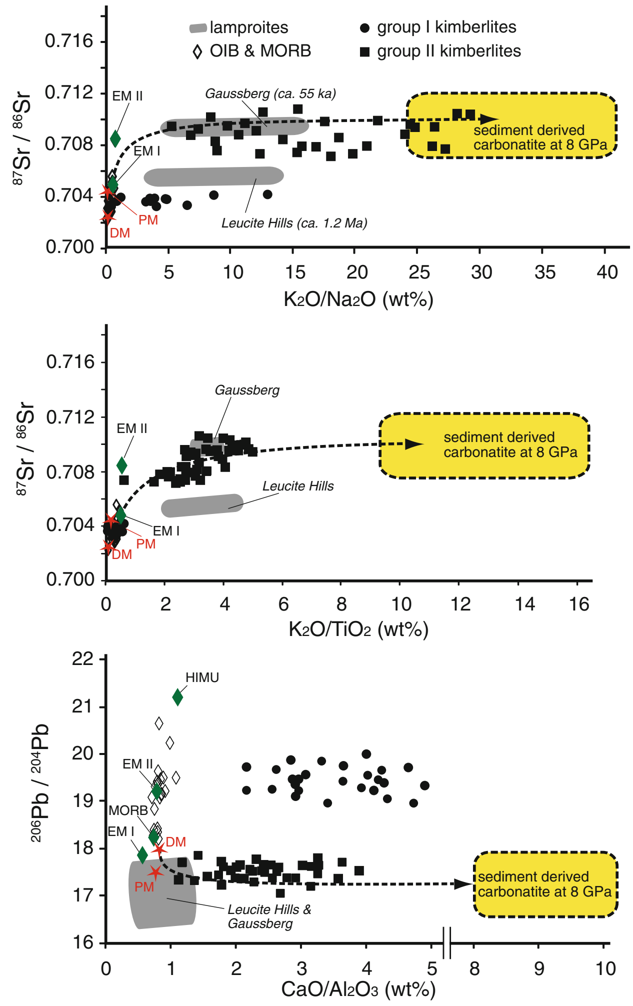

Fig. 12 Major element wt ratios vs. radiogenic isotope composition for OIB & MORB (Jackson and Dasgupta 2008), group I and group II kimberlites (Le Roex et al. 2003; Becker and Le Roex 2006; Coe et al. 2008) and lamproites (Gaussberg, Murphy et al. 2002; Leucite Hills, Mirnejad and Bell 2006). The isotopic composition for the sediment-derived melt used for mixing is from 1.5 Ga old sediment (after 1.4 Ga evolution for a ^{87}Rb/^{86}Sr ratio of 0.2) consisting of 90 wt% pelagic sediment with an initial ^{87}Sr/^{86}Sr$_i$ of 0.7074 (Rehkamper and Hofmann 1997) and 10 wt% marine carbonates with an initial ^{87}Sr/^{86}Sr$_i$ of 0.706 and a Sr concentration 10 times higher than in the pelagic component (Mirota and Veizer 1994; Plank and Langmuir 1996). The Sr (2,000 ppm) and Pb (10 ppm) concentrations of the melt employed to calculate the mixing lines are in agreement with the results of Grassi (2010) and with subduction-related fractionation after Kelley et al. (2005). Values for the depleted mantle and primitive mantle are after Rehkamper and Hofmann (1997) and Hofmann (1988), respectively. **a**,**b** ^{87}Sr/^{86}Sr vs. K_2O/Na_2O and K_2O/TiO_2 showing a good positive correlation as was already recognized for OIB (Jackson and Dasgupta 2008) and in particular for the EM types (Spandler et al. 2010). Note the compositions of group II kimberlites lying on the mixing line depleted mantle sediment–derived 8 GPa carbonatites. **c** ^{206}Pb/^{204}Pb vs. CaO/Al_2O_3 with group II kimberlites lying exactly on the mixing line depleted mantle sediment–derived 8 GPa carbonatites

extremely enriched in potassium, and are characterized by sedimentary and subduction-related geochemical signatures inherited from their source and subduction history. In the clan of ultramafic ultrapotassic rocks, group I kimberlites are the most enriched in CO_2 followed by group II kimberlites and by lamproites, which indicate comparatively low CO_2 contents. This observation shows a positive correlation with the CaO/Al_2O_3 wt% ratio (Fig. 12c) of these magmas and with the CaO content within a single rock type (Becker and Le Roex 2006; Coe et al. 2008). The higher amounts of CaO for a given SiO_2 content observed in group II kimberlites could thus be ascribed to the metasomatic effect of carbonatites with higher X^*_{Ca}, as the ones generated from carbonated sediments (Fig. 6c, d). Figure 12 shows the positive correlation between the potassium enrichment and the radiogenic ^{87}Sr/^{86}Sr isotopic composition of group II kimberlites thus linking both characteristics with a single subduction-related metasomatic process involving a sedimentary source.

Conclusion

When heating subducted carbonated pelites towards a mantle adiabat, melting results into alkaline dolomitic to ferro-magnesian carbonatites that provide a genetic link between CO_2 and potassic metasomatism of the mantle. Residual jadeite in the pelite holds back Na and strongly fractionates the K/Na ratios, leading to an ultrapotassic character of the melts. When entering the mantle, the relatively oxidized carbonatites will react with the relatively reduced mantle forming diamond and K_2O- and CO_2-rich metasomatic zones, which are the most likely source regions for highly potassic kimberlites.

Acknowledgments We are thankful to E. Franzolin, A. Galli and U. Mann for discussions improving the manuscript. Thanks to E. Reusser, for assistance in the microprobe, to A. Rohrbach and C. Liebske for technical support in the laboratory, E. Franzolin and A. Galli for solving computer problems, and to U. Graber, B. Zürcher and A. Jallas for mechanical support. This study was made possible through grant SNF-200020-120006/1. Constructive review by M. Hirschmann improved the final version of the manuscript.

References

Agashev AM, Pokhilenko NR, Takazawa E, McDonald JA, Vavilov MA, Watanabe I, Sobolev NV (2008) Primary melting sequence of a deep (>250 km) lithospheric mantle as recorded in the geochemistry of kimberlite-carbonatite assemblages, Snap Lake dyke system, Canada. Chem Geol 255:317–328

Akaogi M, Ito E, Navrotsky A (1989) Olivine-modified spinel-spinel transitions in the system $MgSiO_4$–$FeSiO_4$-calorimetric measurements, thermochemical calculation, and geophysical application. J Geophys Res 94:15671–15685

Becker M, Le Roex AP (2006) Geochemistry of South African on- and off-craton, Group I and Group II kimberlites: petrogenesis and source region evolution. J Petrol 47:673–703

Brey GP, Bulatov VK, Girnis AV, Lahaye Y (2008) Experimental melting of carbonated peridotite at 6–10 GPa. J Petrol 49:797–821

Brey GP, Bulatov VK, Girnis AV (2009) Influence of water and fluorine on melting of carbonated peridotite at 6 and 10 GPa. Lithos 112:249–259

Buob A, Luth RW, Schmidt MW, Ulmer P (2006) Experiments on $CaCO_3$–$MgCO_3$ solid solutions at high pressure and temperature. Am Mineral 91:435–440

Cartigny P (2005) Stable isotopes and the origin of diamond. Elements 1:79–84

Coe N, Le Roex A, Gurney J, Pearson DG, Nowell G (2008) Petrogenesis of the Swartruggens and Star Group II kimberlite dyke swarms, South Africa: constraints from whole rock geochemistry. Contrib Mineral Petrol 156:627–652

Connolly JAD (2005) Computation of phase equilibria by linear programming: a tool for geodynamic modeling and its application to subduction zone decarbonation. Earth Planet Sci Lett 236:524–541

Dalton JA, Presnall DC (1998) Carbonatitic melts along the solidus of model lherzolite in the system CaO–MgO–Al_2O_3–SiO_2–CO_2 from 3 to 7 GPa. Contrib Mineral Petrol 131:123–135

Dalton JA, Wood BJ (1993) The composition of primary carbonate melts and their evolution through wallrock reaction in the mantle. Earth Planet Sci Lett 119:511–525

Dasgupta R, Hirschmann MM (2006) Melting in the Earth's deep upper mantle caused by carbon dioxide. Nature 440:659–662

Dasgupta R, Hirschmann MM (2007) A modified iterative sandwich method for determination of near-solidus partial melt compositions. II. Application to determination of near-solidus melt compositions of carbonated peridotite. Contrib Mineral Petrol 154:647–661

Dasgupta R, Hirschmann MM, Withers AC (2004) Deep global cycling of carbon constrained by the solidus of anhydrous, carbonated eclogite under upper mantle conditions. Earth Planet Sci Lett 227:73–85

Dasgupta R, Hirschmann MM, Dellas N (2005) The effect of bulk composition on the solidus of carbonated eclogite from partial melting experiments at 3 GPa. Contrib Mineral Petrol 149:288–305

Dasgupta R, Hirschmann MM, Stalker K (2006) Immiscible transition from carbonate-rich to silicate-rich melts in the 3 GPa melting interval of eclogite plus CO_2 and genesis of silica-undersaturated ocean island lavas. J Petrol 47:647–671

Dawson JB (1984) The mantle and crust-mantle relationship. In: Kornprobst J (ed) Kimberlites II. Elsevier, Amsterdam, pp 289–294

Dobrzhinetskaya LF, Green HW (2007) Experimental studies of mineralogical assemblages of metasedimentary rocks at Earth's mantle transition zone conditions. J Met Geol 25:83–96

Domanik KJ, Holloway JR (1998) Experimental synthesis and phase relations of phengitic muscovite from 6.5 to 11 GPa in a calcareous metapelite from the Dabie Mountains, China. In: International workshop on UHP metamorphism and exhumation, Stanford, pp 51–77

Eggleton RA, Boland JN, Ringwood AE (1978) High-pressure synthesis of a new aluminium silicate—$Al_5Si_5O_{17}(OH)$. Geochem J 12:191–194

Falloon TJ, Green DH, O'Neill HS, Hibberson WO (1997) Experimental tests of low degree peridotite partial melt compositions: implications for the nature of anhydrous near-solidus peridotite melts at 1 GPa. Earth Planet Sci Lett 152:149–162

Faure G (2000) Origin of igneous rocks: the isotopic evidence. Springer, Berlin

Foley S (1992) Vein-plus-wall-rock melting mechanism in the lithosphere and the origin of potassic alkaline magmas. Lithos 28:435–453

Foley SF, Yaxley GM, Rosenthal A, Buhre S, Kiseeva ES, Rapp RP, Jacob DE (2009) The composition of near-solidus melts of peridotite in the presence of CO_2 and H_2O between 40 and 60 kbar. Lithos 112:274–283

Francis D, Patterson M (2009) Kimberlites and aillikites as probes of the continental lithospheric mantle. Lithos 109:72–80

Franzolin E, Schmidt M, Poli S (2010) Ternary Ca–Fe–Mg carbonates: subsolidus phase relations at 3.5 GPa and a thermodynamic solid solution model including order/disorder. Contrib Mineral Petrol. doi:10.1007/s00410-010-0527-x

Freestone IC, Hamilton DL (1980) The role of liquid immiscibility in the genesis of carbonatites—an experimental-study. Contrib Mineral Petrol 73:105–117

Frost DJ, McCammon CA (2008) The redox state of Earth's mantle. Annu Rev Earth Planet Sci 36:389–420

Genge MJ, Jones AP, Price GD (1995) An infrared and Raman-study of carbonate glasses—implications for the structure of carbonatite magmas. Geochim Cosmochim Acta 59:927–937

Ghosh S, Ohtani E, Litasov KD, Terasaki H (2009) Solidus of carbonated peridotite from 10 to 20 GPa and origin of magnesiocarbonatite melt in the Earth's deep mantle. Chem Geol 262:17–28

Girnis AV, Bulatov VK, Lahaye Y, Brey GP (2006) Partitioning of trace elements between carbonate–silicate melts and mantle minerals: experiment and petrological consequences. Petrology 14:492–514

Grassi D (2010) Melting of subducted carbonated pelites from 5 to 23 GPa: alkali-carbonatites, mantle metasomatism, and element recycling. Dissertation, ETH Zurich

Green DH, Wallace ME (1988) Mantle metasomatism by ephermal carbonatite melts. Nature 336:459–462

Guzmics T, Kodolanyi J, Kovacs I, Szabo C, Bali E, Ntaflos T (2008) Primary carbonatite melt inclusions in apatite and in K-feldspar of clinopyroxene-rich mantle xenoliths hosted in lamprophyre dikes (Hungary). Mineral Petrol 94:225–242

Hammouda T (2003) High-pressure melting of carbonated eclogite and experimental constraints on carbon recycling and storage in the mantle. Earth Planet Sci Lett 214:357–368

Hammouda T, Laporte D (2000) Ultrafast mantle impregnation by carbonatite melts. Geology 28:283–285

Hermann J, Spandler CJ (2008) Sediment melts at sub-arc depths: an experimental study. J Petrol 49:717–740

Hirschmann MM (2000) Mantle solidus: experimental constraints and the effects of peridotite composition. Geochem Geophys Geosyst 1:1042–1067

Hirschmann MM, Dasgupta R (2007) A modified iterative sandwich method for determination of near-solidus partial melt compositions. I. Theoretical considerations. Contrib Mineral Petrol 154:635–645

Hirschmann MM, Aubaud C, Withers AC (2005) Storage capacity of H_2O in nominally anhydrous minerals in the upper mantle. Earth Planet Sci Lett 236:167–181

Hofmann AW (1988) Chemical differentiation of the Earth—the relationship between mantle, continental-crust and oceanic-crust. Earth Planet Sci Lett 90:297–314

Irving AJ, Wyllie PJ (1975) Subsolidus and melting relationships for calcite, magnesite and join $CaCO_3$–$MgCO_3$ to 36 kb. Geochim Cosmochim Acta 39:35–53

Jackson MG, Dasgupta R (2008) Compositions of HIMU, EM1, and EM2 from global trends between radiogenic isotopes and major elements in ocean island basalts. Earth Planet Sci Lett 276:175–186

Kamenetsky MB, Sobolev AV, Kamenetsky VS, Maas R, Danyushevsky LV, Thomas R, Pokhilenko NP, Sobolev NV (2004) Kimberlite melts rich in alkali chlorides and carbonates: a potent metasomatic agent in the mantle. Geology 32:845–848

Kawamoto T, Hervig RL, Holloway JR (1996) Experimental evidence for a hydrous transition zone in the early Earth's mantle. Earth Planet Sci Lett 142:587–592

Kelley KA, Plank T, Farr L, Ludden J, Staudigel H (2005) Subduction cycling of U, Th, and Pb. Earth Planet Sci Lett 234:369–383

Keppler H, Smyth JR (2006) Water in nominally anhydrous minerals. Rev Mineral Geochem 62:1–478

Kerrick DM, Connolly JAD (2001) Metamorphic devolatilization of subducted marine sediments and the transport of volatiles into the Earth's mantle. Nature 411:293–296

Keshav S, Gudfinnsson GH (2010) Experimentally dictated stability of carbonated oceanic crust to moderately great depths in the Earth: results from the solidus determination in the system CaO–MgO–Al2O_3–SiO_2–CO_2. J Geophys Res 115:B05205. doi:10.1029/2009JB006457

Kessel R, Schmidt MW, Ulmer P, Pettke T (2005a) Trace element signature of subduction-zone fluids, melts and supercritical liquids at 120–180 km depth. Nature 437:724–727

Kessel R, Ulmer P, Pettke T, Schmidt MW, Thompson AB (2005b) The water-basalt system at 4–6 GPa: phase relations and second critical endpoint in a K-free eclogite at 700–1400°C. Earth Planet Sci Lett 237:873–892

Kincaid C, Sacks IS (1997) Thermal and dynamical evolution of the upper mantle in subduction zones. J Geophys Res 102:12295–12315

Klein-BenDavid O, Izraeli ES, Hauri E, Navon O (2007) Fluid inclusions in diamonds from the Diavik mine, Canada and the evolution of diamond-forming fluids. Geochim Cosmochim Acta 71:723–744

Kohara S, Badyal YS, Koura N, Idemoto Y, Takahashi S, Curtiss LA, Saboungi ML (1998) The structure of molten alkali carbonates studied by neutron diffraction and ab initio calculations. J Phys Cond Matt 10:3301–3308

Komabayashi T, Omori S, Maruyama S (2004) Petrogenetic grid in the system MgO–SiO_2–H_2O up to 30 GPa, 1600°C: applications to hydrous peridotite subducting into the Earth's deep interior. J Geophys Res 109:1–12

Konzett J, Fei YW (2000) Transport and storage of potassium in the Earth's upper mantle and transition zone: an experimental study to 23 GPa in simplified and natural bulk compositions. J Petrol 41:583–603

Korsakov AV, Hermann J (2006) Silicate and carbonate melt inclusions associated with diamonds in deeply subducted carbonate rocks. Earth Planet Sci Lett 241:104–118

Le Roex AP, Bell DR, Davis P (2003) Petrogenesis of group I kimberlites from Kimberley, South Africa: evidence from bulk-rock geochemistry. J Petrol 44:2261–2286

Litasov KD, Ohtani E (2009) Solidus and phase relations of carbonated peridotite in the system CaO–Al_2O_3–MgO–SiO_2–Na_2O–CO_2 to the lower mantle depths. Phys Earth Plan Int 177:46–58

Litasov KD, Kagi H, Shatskly A, Ohtani E, Lakshtanov DL, Bass JD, Ito E (2007) High hydrogen solubility in A1-rich stishovite and water transport in the lower mantle. Earth Planet Sci Lett 262:620–634

Luth RW (2001) Experimental determination of the reaction aragonite plus magnesite = dolomite at 5–9 GPa. Contrib Mineral Petrol 141:222–232

McCandless TE (1999) Kimberlites: mantle expressions of deep-seated subduction. In: Gurney JJ, Gurney JL, Pascoe MD, Richardson SH (eds) Proceedings of the 7th international kimberlite conference, vol 2. Red Roof Publishers, Cape Town, pp 545–549

Mirnejad H, Bell K (2006) Origin and source evolution of the Leucite Hills lamproites: evidence from Sr–Nd–Pb–O isotopic compositions. J Petrol 47:2463–2489

Mirota MD, Veizer J (1994) Geochemistry of precambrian carbonates: VI. Aphebian Albanel formations, Quebec, Canada. Geochim Cosmochim Acta 58:1735–1745

Mitchell RH (1995) Kimberlites. Mineral geochem petrol. Plenum Press, New York, p 442

Mitchell RH (2005) Carbonatites and carbonatites and carbonatites. In: Joint Annual meeting of the geological-association-of-Canada/mineralogical-association-of-Canada. Mineralogical Association of Canada, Halifax, pp 2049–2068

Molina JF, Poli S (2000) Carbonate stability and fluid composition in subducted oceanic crust: an experimental study on H_2O–CO_2-bearing basalts. Earth Planet Sci Lett 176:295–310

Morishima H, Kato T, Suto M, Ohtani E, Urakawa S, Utsumi W, Shimomura O, Kikegawa T (1994) The phase-boundary between α-Mg2SiO4 and β-MgSiO4 determined by in situ X-ray-observation. Science 265:1202–1203

Murphy DT, Collerson KD, Kamber BS (2002) Lamproites from Gaussberg, Antarctica: possible transition zone melts of Archaean subducted sediments. J Petrol 43:981–1001

Nichols GT, Wyllie PJ, Stern CR (1994) Subduction zone-melting of pelagic sediments constrained by melting experiments. Nature 371:785–788

Okamoto K, Maruyama S (2004) The eclogite-garnetite transformation in the MORB + H_2O system. Phys Earth Plan Int 146:283–296

Ono S (1998) Stability limits of hydrous minerals in sediment and mid-ocean ridge basalt compositions: implications for water transport in subduction zones. J Geophys Res 103:18253–18267

Palyanov YN, Shatsky VS, Sobolev NV, Sokol AG (2007) The role of mantle ultrapotassic fluids in diamond formation. Proc Natl Acad Sci USA 104:9122–9127

Peacock SM (2003) Thermal structure and metamorphic evolution of subducting slab. In: Eiler J (ed) Inside the subduction factory, vol 138. American Geophysical Union, Washington, DC, pp 7–22

Plank T, Langmuir CH (1996) The chemical composition of subducting sediment and its consequences for the crust and mantle. In: Workshop on geochemical earth reference model, Lyon, pp 325–394

Poli S, Schmidt MW (2002) Petrology of subducted slabs. Annu Rev Earth Planet Sci 30:207–235

Rapp RP, Irifune T, Shimizu N, Nishiyama N, Norman MD, Inoue J (2008) Subduction recycling of continental sediments and the origin of geochemically enriched reservoirs in the deep mantle. Earth Planet Sci Lett 271:14–23

Rehkamper M, Hofmann AW (1997) Recycled ocean crust and sediment in Indian Ocean MORB. Earth Planet Sci Lett 147:93–106

Rohrbach A, Schmidt MW, Ballhaus C (2009) Carbonate stability in the Earth's lower mantle and redox melting across the 660 km discontinuity. Geochim Cosmochim Acta 73:A1113

Sano A, Ohtani E, Kubo T, Funakoshi K (2003) In situ X-ray observation of decomposition of hydrous aluminum silicate $AlSiO_3OH$ and aluminum oxide hydroxide δ-AlOOH at high pressure and temperature. J Phys Chem Solid 65:1547–1554

Schmidt MW, Poli S (1998) Experimentally based water budgets for dehydrating slabs and consequences for arc magma generation. Earth Planet Sci Lett 163:361–379

Schmidt MW, Ulmer P (2004) A rocking multianvil: elimination of chemical segregation in fluid-saturated high-pressure experiments. Geochim Cosmochim Acta 68:1889–1899

Schmidt MW, Poli S, Comodi P, Zanazzi PF (1997) High-pressure behavior of kyanite: decomposition of kyanite into stishovite and corundum. Am Mineral 82:460–466

Schmidt MW, Finger LW, Angel RJ, Dinnebier RE (1998) Synthesis, crystal structure, and phase relations of $AlSiO_3OH$, a high-pressure hydrous phase. Am Mineral 83:881–888

Schmidt MW, Vielzeuf D, Auzanneau E (2004) Melting and dissolution of subducting crust at high pressures: the key role of white mica. Earth Planet Sci Lett 228:65–84

Spandler C, Yaxley G, Green DH, Scott D (2010) Experimental phase and melting relations of metapelite in the upper mantle: implications for the petrogenesis of intraplate magmas. Contrib Mineral Petrol 160:569–589

Susaki J, Akaogi M, Akimoto S, Shimomura O (1985) Garnet-perovskit transformation in $CaGeO_3$—in situ X-ray measurements using synchrotron radiation. Geophys Res Lett 12:729–732

Taniguchi T, Dobson D, Jones AP, Rabe R, Milledge HJ (1996) Synthesis of cubic diamond in the graphite-magnesium carbonate and graphite-$K_2Mg(CO_3)_2$ systems at high pressure of 9–10 GPa region. J Mat Res 11:2622–2632

Thibault Y, Edgar AD, Lloyd FE (1992) Experimental investigation of melts from a carbonated phlogopite lherzolite—implications for metasomatism in the continental lithospheric mantle. Am Mineral 77:784–794

Thomsen TB, Schmidt MW (2008a) The biotite to phengite reaction and mica-dominated melting in fluid carbonate-saturated pelites at high pressures. J Petrol 49:1889–1914

Thomsen TB, Schmidt MW (2008b) Melting of carbonated pelites at 2.5–5.0 GPa, silicate–carbonatite liquid immiscibility, and potassium-carbon metasomatism of the mantle. Earth Planet Sci Lett 267:17–31

Tomlinson EL, Jones AP, Harris JW (2006) Co-existing fluid and silicate inclusions in mantle diamond. Earth Planet Sci Lett 250:581–595

van Achterbergh E, Griffin WL, Ryan CG, O'Reilly SY, Pearson NJ, Kivi K, Doyle BJ (2002) Subduction signature for quenched carbonatites from the deep lithosphere. Geology 30:743–746

van Achterbergh E, Griffin WL, Ryan CG, O'Reilly SY, Pearson NJ, Kivi K, Doyle BJ (2003) Melt inclusions from the deep Slave lithosphere: implications for the origin and evolution of mantle-derived carbonatite and kimberlite. In: 8th international kimberlite conference, Victoria, pp 461–474

van Keken PE, Kiefer B, Peacock SM (2002) High-resolution models of subduction zones: implications for mineral dehydration reactions and the transport of water into the deep mantle. Geochem Geophys Geosyst 3:1056–1076

Vervoort JD, Blichert-Toft J (1999) Evolution of the depleted mantle: Hf isotope evidence from juvenile rocks through time. Geochim Cosmochim Acta 63:533–556

Wallace ME, Green DH (1988) An experimental-determination of primary carbonatite magma composition. Nature 335:343–346

Walter MJ, Bulanova GP, Armstrong LS, Keshav S, Blundy JD, Gudfinnsson G, Lord OT, Lennie AR, Clark SM, Smith CB, Gobbo L (2008) Primary carbonatite melt from deeply subducted oceanic crust. Nature 454:622–630

Wu Y, Fei YW, Jin ZM, Liu XY (2009) The fate of subducted upper continental crust: an experimental study. Earth Planet Sci Lett 282:275–284

Wunder B, Rubie DC, Ross CR, Medenbach O, Seifert F, Schreyer W (1993) Synthesis, stability, and properties of $Al_2SiO_4(OH)_2$—a fully hydrated analog of topaz. Am Mineral 78:285–297

Wyllie PJ (1988) Magma genesis, plate-tectonics, and chemical differentiation of the Earth. Rev Geophys 26:370–404

Wyllie PJ, Sekine T T (1982) The formation of mantle phlogopite in subduction zone hybridization. Contrib Mineral Petrol 79:375–380

Yagi T, Akimoto SI (1976) Direct determination of coesite-stishovite transition by in situ X-ray measurements. Tectonophys 35:259–270

Yasuda A, Fujii T, Kurita K (1994) Melting phase-relations of an anhydrous midocean ridge basalt from 3 to 20 GPa—implications for the behaviour of subducted oceanic-crust in the mantle. J Geophys Res 99:9401–9414

Yaxley GM, Brey GP (2004) Phase relations of carbonate-bearing eclogite assemblages from 2.5 to 5.5 GPa: implications for petrogenesis of carbonatites. Contrib Mineral Petrol 146:606–619

Yaxley GM, Green DH (1994) Experimental demonstration of refractory carbonate-bearing eclogite and siliceous melt in the subduction regime. Earth Planet Sci Lett 128:313–325

Yaxley GM, Green DH (1996) Experimental reconstruction of sodic dolomitic carbonatite melts from metasomatised lithosphere. Contrib Mineral Petrol 124:359–369

Yong WJ, Dachs E, Withers AC, Essene EJ (2006) Heat capacity and phase equilibria of hollandite polymorph of $KAlSi_3O_8$. Phys Chem Mineral 33:167–177

Zhang J, Li B, Utsumi W, Liebermann RC (1996) In situ X-ray observations of the coesite stishovite transition: reversed phase boundary and kinetics. Phys Chem Mineral 23:1–10